May 10, 2018

Computational Study of Hydrogel Ring Device for Ocular Drug Delivery

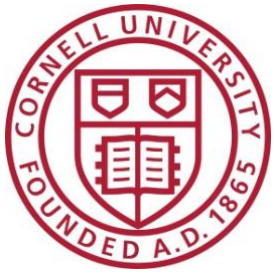

BEE 4530/Group 03

Sarah Hanif
Abigail Lim
Hilarie Sit
Wan Qing Melissa Tan

Department of Biological and Environmental Engineering
Cornell University, Ithaca, NY

Table of Contents

1 Executive Summary

Researchers have developed many different kinds of ocular drug delivery devices. However, most address anterior eye disorders—very few are designed specifically for the treatment of posterior eye diseases. A recently-developed hydrogel ring device is capable of delivering therapeutic quantities of the drug Ofloxacin to treat ocular infections at the back of the eye—a region typically difficult to access via systemic (e.g. ingestion of pills) and topical (e.g. eye drops) methods. Despite promising preliminary *in vivo* test results, much remains unknown about the precise drug transport pathway from the hydrogel ring to the posterior segment of the eye, as well as how design parameters may be altered to increase drug delivery efficiency. The aim of this work is to fully characterize the drug release and transport characteristics from the hydrogel, to ocular tissues (anterior and posterior), as well as provide a quantitative method for the optimization of various hydrogel ring design parameters.

To achieve the abovementioned goals, we built a computational model using COMSOL Multiphysics to simulate the release of Ofloxacin from the hydrogel ring and to obtain the resulting drug distribution in ocular tissues at various time points. Using the model, we monitored the transient Ofloxacin concentration profile over the entire eye, for a treatment period of ten hours. Our results showed that while Ofloxacin diffuses to the anterior region much more quickly than to posterior tissues, Ofloxacin concentrations do successfully accumulate to therapeutic levels in the posterior tissues during the simulated ten-hour treatment period. This finding supports the therapeutic potential of the hydrogel ring for the treatment of posterior eye diseases.

We also performed optimization analyses to determine the ideal set of hydrogel ring design parameters for the treatment of infections caused by three bacterial species commonly associated with ocular disorders: *Escherichia coli*, *Staphylococcus aureus*, and *Streptococcus pneumoniae.* Preliminary findings suggest that the combination of an initial mass of $3mg/m^3$ of Ofloxacin in the hydrogel and an Ofloxacin diffusivity of $3.11 \cdot 10^{-9} m^2/s$ in the hydrogel provide the best possible therapeutic outcome (from the range of values tested) for the treatment of *E. coli* and *S. aureus* infections.

To our best knowledge, there is no existing computational model that simulates drug transport through the entire human eye from an ocular drug delivery device. We believe that our computational model will be highly useful for quantitative device characterization of the hydrogel ring, as well as in the optimization of the hydrogel ring design for the treatment of posterior eye disorders. This work may also serve as a model and reference for future computational work on ocular pharmacokinetics and/or ocular drug delivery devices.

Keywords: ocular drug delivery, hydrogel, ocular ring, computational model, finite element analysis, COMSOL, ocular pharmacokinetics.

2 Introduction

Despite many innovations over the last few decades, the search for safer, more effective and more convenient methods for ocular drug delivery remains an ongoing one [1]–[5] . As in the design of any drug delivery system, engineers must ensure: (1) biocompatibility of the drug delivery devices, (2) controlled, sustained release of drugs to target tissues, and (3) patient comfort [1], [5]. In addition to these general concerns, however, the design process for ocular drug delivery is further complicated by the complex physical composition of the human eye and its high sensitivity to foreign materials [1], [5], [6]. The relative impermeability of various ocular tissues (e.g. cornea and lens) also presents a major obstacle to efficient drug transport to posterior eye segments, especially in cases of bacterial infections or diseases that afflict regions of the eye that lie far from the cornea [1], [5], [6]. A high initial drug concentration in the delivery device may allow for drug levels in posterior tissues to accumulate to the Minimum Inhibitory Concentration (MIC) necessary for the effective treatment of bacterial infections. However, this approach may result in overly high (and potentially toxic) drug concentrations in ocular tissues nearer to the device during the treatment period [1], [5], [6].

[6] has recently reported on a new design for a hydrogel ring device that is capable of delivering therapeutic quantities of the bactericidal drug Ofloxacin to treat ocular infections at the back of the eye—a region typically difficult to access via systemic (e.g. ingestion of pills) and topical (e.g. eye drops) methods [1], [5]–[7]. The hydrogel ring is made from 2-Hydroxyethyl methacrylate (HEMA), a non-biodegradable polymer often employed in ophthalmic applications [6]. Unlike other drug-eluting hydrogel contact lens, the proposed hydrogel ring has a cornea-shaped cut-out in the center, so as to minimize contact with the cornea and thus reduce the risk of a drug overaccumulation in the cornea (which would lead to corneal disorders) [6]. Results from *in vitro* experiments on rabbits showed that the proposed hydrogel ring design (referenced as Ring 1 in [6]) provided the best therapeutic outcome when compared to controls (i.e. corneal lens, scleral/corneal lens, and topically-applied ofloxacin ophthalmic solution). The newly-developed hydrogel ring significantly increased Ofloxacin concentrations in posterior tissues, while reducing Ofloxacin concentrations in anterior regions [6]. These results strongly suggest the therapeutic potential of the hydrogel ring in the treatment of posterior eye disorders.

3 Problem Statement

Notwithstanding the promising preliminary *in vivo* test results, much remains unknown about the precise drug transport pathway from the hydrogel to the posterior segment of the eye, as well as how design parameters may be altered to increase drug delivery efficiency. Prior *in vivo* experiments reported in [6] do not provide information on the spatial distribution of the delivered drug in ocular tissues during treatment. Without detailed characterization of the device, it is difficult for further design optimization to improve drug delivery efficiency, and to extend compatibility of the device with a wider range of pharmaceuticals that can be used to treat ocular diseases. *In vivo* experiments are also resource-intensive and time-consuming, and thus are not a feasible means for future optimization studies of the hydrogel ring design, especially if they require a high volume of iterations and trials.

Unlike traditional means of *in vivo* and *in vitro* testing, computational models are less time-consuming and resource-demanding, and also provides users with the flexibility to tune specific parameters and/or study specific biological processes [2], [8]–[10]. We thus designed and performed a computational study of the drug-eluting hydrogel ring in [6], so as to provide quantitative device characterization and facilitate future design and optimization work.

4 Design Objectives

The specific goals of our computational study are as follows:

- Build an anatomically-accurate computational model for ocular pharmacokinetics testing that incorporates the relevant physics influencing drug transport in the eye
- Map the transient concentration profile of Ofloxacin over the entire eye for a treatment period of ten hours
- Validate the computed solution (derived from the model) with experimental data in [6]
- Optimize selected design parameters (initial mass of Ofloxacin loaded into hydrogel and diffusivity of Ofloxacin in the hydrogel) for optimal drug delivery to treat bacterial infections in the posterior region

In achieving these design objectives, we hope that our computational model would be able to verify the therapeutic potential of the drug-eluting hydrogel ring to treat posterior segment ocular disorders, as well as facilitate further computational work on ocular pharmacokinetics and/or design of ocular drug delivery devices.

5 Computational Model

5.1 Problem Formulation

To address the above research goals, we developed a 2D-axisymmetric finite element computational model in COMSOL Multiphysics® Version 5.3 (COMSOL Inc., Stockholm, Sweden), which simulates the release of Ofloxacin from the hydrogel ring and provides the spatial distribution of Ofloxacin within ocular tissues during the treatment period (Figure 1). The model integrates existing computational work on drug diffusion within the anterior and posterior segments of the eye and incorporates four physics: (1) heat transport within the eye, (2) density-driven natural convection flow of aqueous humor, (3) pressure-driven Darcy flow through the vitreous, and (4) transport of a diluted species within the entire eye (Figures 2, 3). We created the computational domain from scratch, using physical dimensions of various ocular tissues and the hydrogel ring provided in research literature (Figure 1). See Appendix 13.1 for physical dimensions used.

We modeled the transport of diluted species (Ofloxacin) through all 13 sub-domains (Figures 1-3). The main complexity in our model is due to the presence of spatially-varying, domain-specific velocities. To obtain the velocity profile in the anterior region of the eye (sub-domains 8 and 9), we coupled the solving of the heat equation with the solving of the Navier-Stokes equation. We applied the Boussinesq approximation (as seen from the temperature-dependent density term in Navier-Stokes equation) to reflect the buoyancy-driven natural convection of aqueous humor in sub-domains 8 and 9 (Figure 1) [8], [11]. Since aqueous humor (i.e. the fluid that flows within sub-domains 8 and 9) is supplied through the ciliary body (sub-domain 12) and drained through the trabecular meshwork (sub-domain 10), we specified sub-domain 12 as the inlet and sub-domain 10 as the outlet. To solve for the velocity profile in the posterior region of the eye (sub-domains 1-4), we solved Darcy's Flow equation, which accounts for the pressure-driven flow through a static, incompressible, porous medium (i.e. the vitreous) [12].

After solving for the respective velocities, we plugged the domain-specific velocity terms into the transport equation and solved the transport equation for all 13 sub-domains.

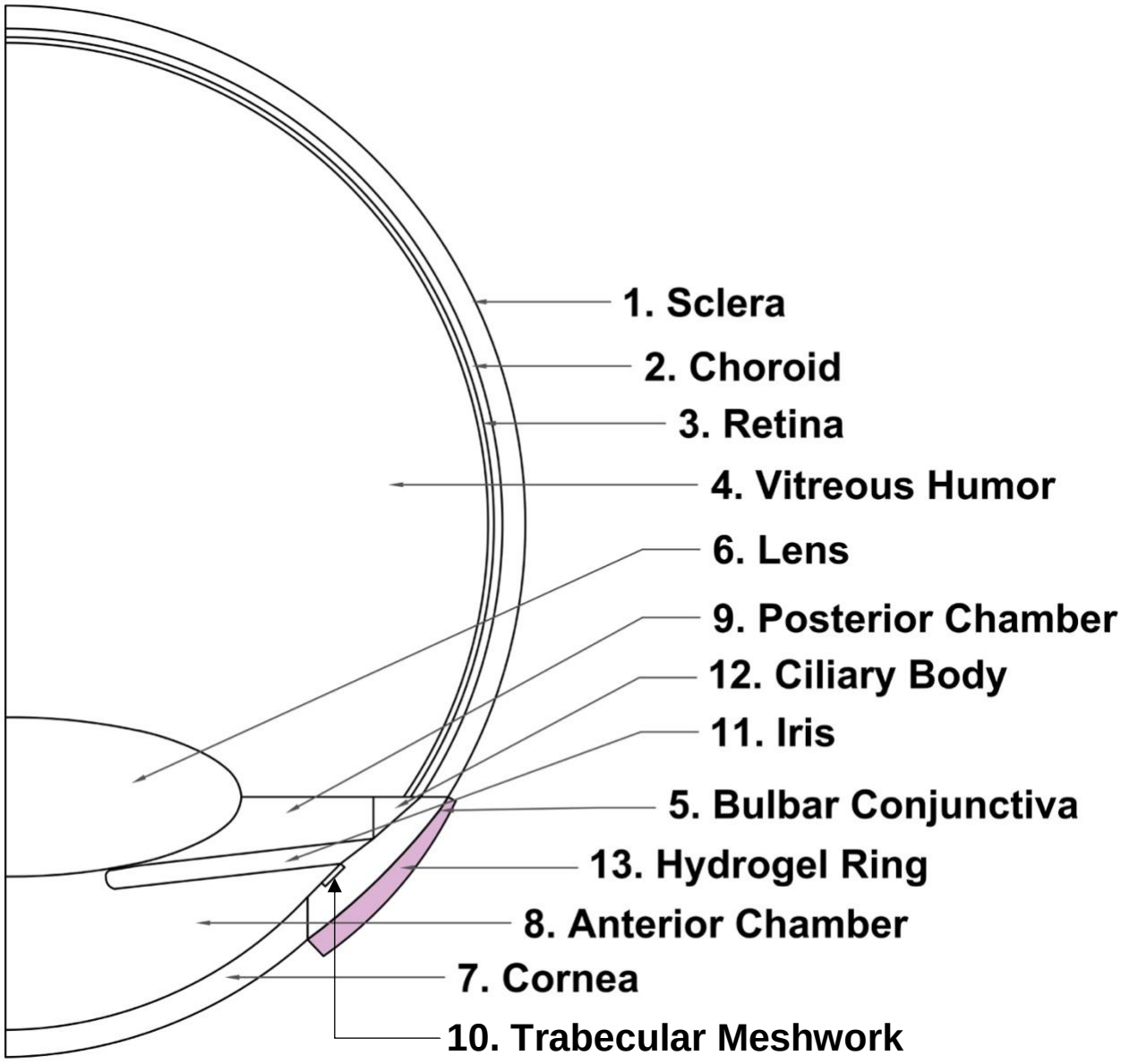

Figure 1. Eye Anatomy with Labeled Sub-Domains. Our computational geometry consists of thirteen sub-domains with anatomically-accurate physical parameters and material properties derived from literature (see Appendix 13.1 to 13.5).

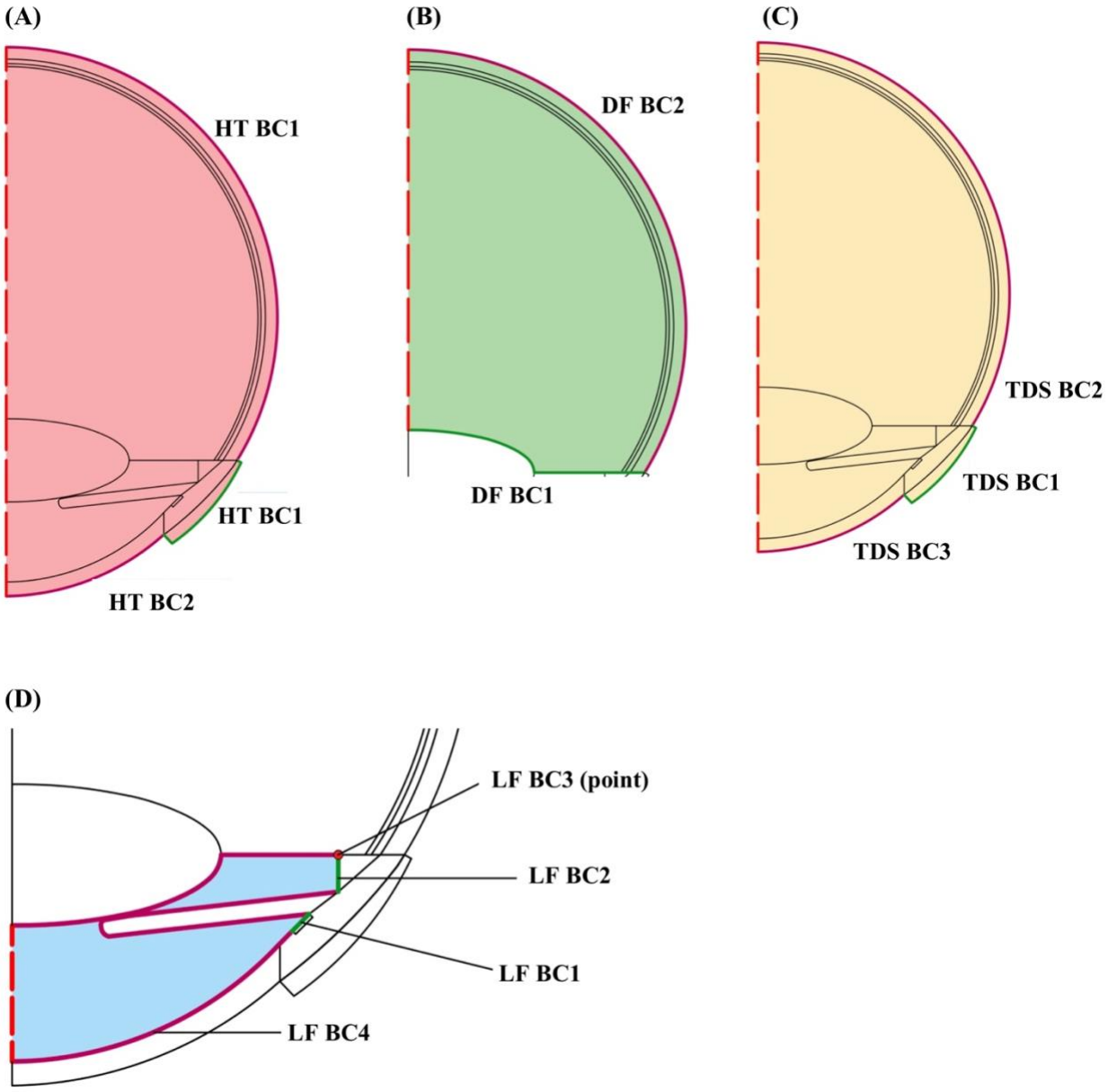

Figure 2. Domain-Specific Physics with Associated Boundary Conditions. (A) heat transfer (HT); (B) Darcy's flow (DF); (C) transport of a diluted species (TDS); (D) laminar flow (LF). The labeled boundary conditions correspond to the boundary conditions described in Figure 3.

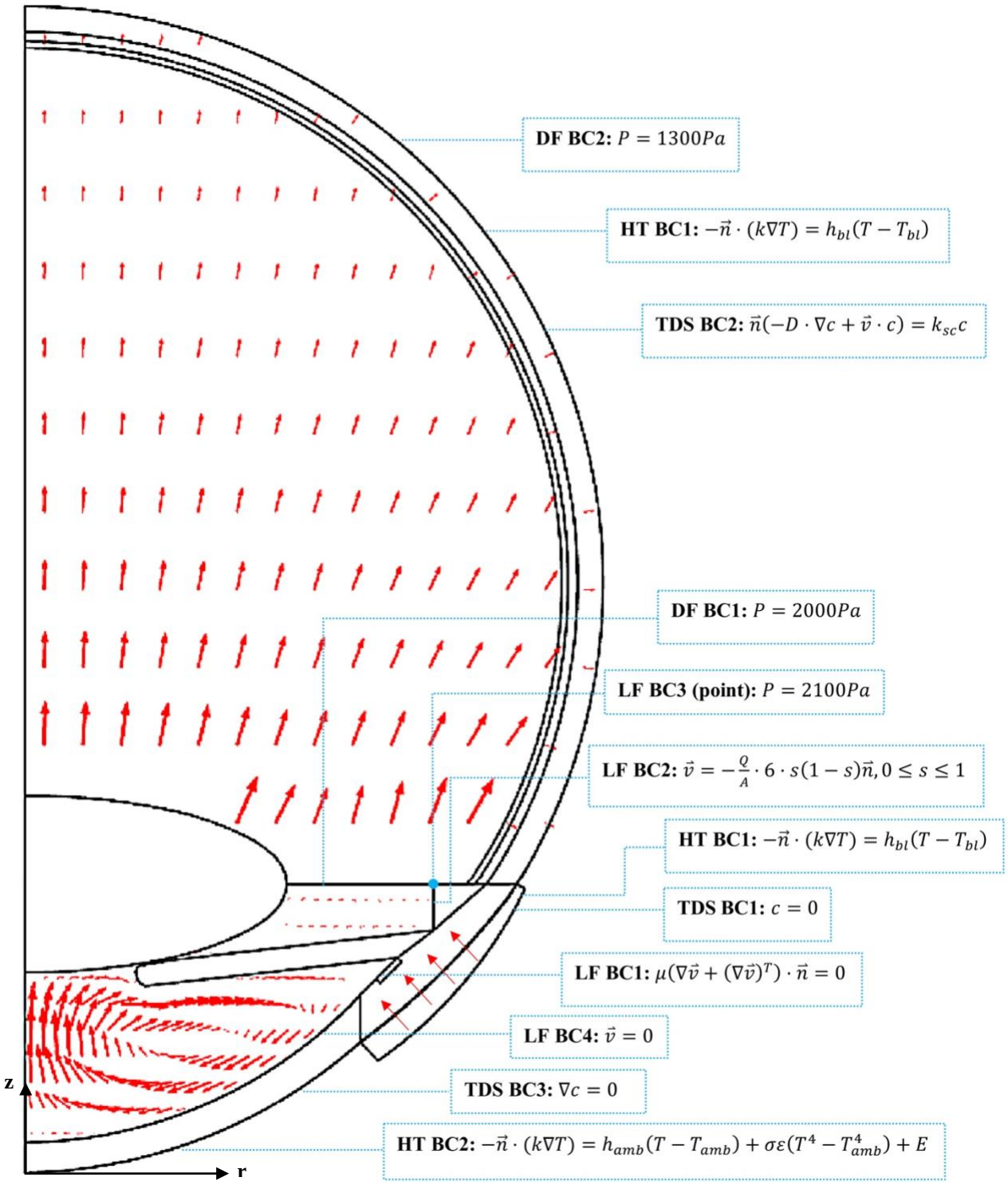

Figure 3. 2D Axisymmetric Computational Domain for COMSOL Implementation with Boundary Conditions for Each of the Four Physics Modules. HT: heat transfer (dependent variable $\boldsymbol{T}$), DF: darcy-driven flow (dependent variables $\vec{\boldsymbol{v}}, \boldsymbol{P}$), LF: laminar flow (dependent variables $\vec{\boldsymbol{v}}, \boldsymbol{P}$), TDS: transport of a diluted species (dependent variable $\boldsymbol{c}$). BCx: boundary condition x (1, 2, 3, or 4). Symmetry boundary condition is imposed on r=0mm for all four physics.

5.2 Simplifications and Assumptions

In order to implement a 2D-axisymmetric geometry, we modeled the specific case in which the patient is in a supine position, i.e. gravity is pointing straight upwards relative to our computational geometry (Figure 1).

We accounted for drug elimination into conjunctival lymphatics and episcleral veins from the scleral surface (sub-domain 1) using k_{sc}, a mass transfer coefficient at the scleral surface [12].

We accounted for drug loss to choroidal circulation (sub-domain 2) using the term $\gamma(c_{bl} - c)$, where γ is the rate constant for volumetric drug transport across the blood vessels in the choroid and c_{bl} is the concentration of the drug in the blood circulation [12]. For simplicity, we assumed that $c_{bl} = 0$ and also ignored drug loss from the retina (sub-domain 3) due to active pumping by the retinal pigment epithelium and retinal capillaries.

6 Governing Equations and Boundary Conditions

6.1 Heat Transfer

Sub-Domains Involved
All

Governing Equation

$$\rho C_p \vec{v} \cdot \nabla T = \nabla \cdot (k \nabla T) \quad (1)$$

(please see Appendix 13.2 for input parameters)

Time Dependence
Steady-state

Boundary Conditions
Flux boundary condition at the external boundary of sub-domain 8 (HT BC2, Figures 2A & 3), accounting for convection, radiative heat transfer, and heat loss by tear evaporation from the cornea, i.e. external boundary of sub-domain 8, to the surrounding air [8]:

$$-\vec{n} \cdot (k \nabla T) = h_{amb}(T - T_{amb}) + \sigma \varepsilon (T^4 - T_{amb}^4) + E \quad (2)$$

where $T_{amb} = 298K$, $h_{amb} = 10W/(m^2 \cdot K)$, $E = 40W/m^2$, $\varepsilon = 0.975$ [8]

Flux boundary condition at all remaining external boundaries (HT BC1, Figures 2A & 3), assuming that the rest of the eye ball and the hydrogel ring are surrounded by blood vessels [8]:

$$-\vec{n} \cdot (k \nabla T) = h_{bl}(T - T_{bl}) \quad (3)$$

where $T_{bl} = 310K$, $h_{bl} = 65W/(m^2 \cdot K)$ [8]

Symmetry boundary condition at $r = 0$ [8]:

$$\frac{\partial T}{\partial r} = 0 \quad (4)$$

6.2 Laminar Flow

Sub-Domains Involved: 8, 9 (Figure 1)

Governing Equations

$$\rho_0(\vec{v}\cdot\nabla)\vec{v} = -\nabla P + \mu\nabla^2\vec{v} + \rho_0\left[1-\beta\left(T-T_{ref}\right)\right]\vec{g} \quad (5)$$

$$\nabla(\rho\vec{v}) = 0 \quad (6)$$

(please see Appendix 13.3 for input parameters)

Time Dependence
Steady-state

Boundary Conditions
No viscous stresses at outlet (LF BC1, Figures 2D & 3) [8]:

$$\mu(\nabla\vec{v} + (\nabla\vec{v})^T)\cdot\vec{n} = 0 \quad (7)$$

Parabolic velocity profile at inlet (LF BC2, Figures 2D & 3) [8]:

$$\vec{v} = -\frac{Q}{A}\cdot 6\cdot s(1-s)\vec{n}, 0 \le s \le 1 \quad (8)$$

Pressure boundary condition at point (6.422,4.539) (LF BC3, Figures 2D & 3) [8]:

$$\mathrm{P} = 2100\mathrm{Pa} \quad (9)$$

No-slip boundary condition at all other boundaries/walls (LF BC4, Figures 2D & 3) [8]:

$$\vec{v} = 0 \quad (10)$$

Symmetry boundary condition at $r = 0$ [8]:

$$\frac{\partial v_r}{\partial r} = 0 \quad (11)$$

6.3 Diffusion Through Porous Media

Sub-Domains Involved
1, 2, 3, 4 (Figure 1)

Governing Equation

$$\vec{v} = -\frac{K}{\mu}\nabla P \tag{12}$$

(please see Appendix 13.4 for input parameters)

Time Dependence
Steady-state

Boundary Conditions
Pressure boundary condition at internal boundary between sub-domains 4 and 9 (DF BC2, Figures 2B & 3) [12]:

$$P = 2000Pa \tag{13}$$

Pressure boundary condition at outer boundary of sub-domain 10 (DF BC1, Figures 2B & 3) [12]:

$$P = 1300Pa \tag{14}$$

6.4 Transport of Diluted Species

Sub-Domains Involved
All

Governing Equation

$$\frac{\partial \mathrm{c}}{\partial \mathrm{t}} + \vec{v} \cdot \nabla \mathrm{c} - \mathrm{D}\,\nabla^2\,\mathrm{c} = \mathrm{k} \tag{15}$$

(please see Appendix 13.5 for input parameters)

Time Dependence
Transient

Boundary Conditions (External)
Concentration boundary condition at boundaries along the two short edges of the bulbar conjunctiva (sub-domain 5) and at the external boundary of sub-domain 13 (TDS BC1, Figures 2C & 3), assuming that these boundaries are exposed to internal blood circulation and any drug at the boundaries are promptly carried away by blood flow:

$$c = 0 \tag{16}$$

Flux boundary condition at external boundary of sub-domain 1 (TDS BC2, Figures 2C & 3) [8], [12]:

$$\vec{n}(-D \cdot \nabla c + \vec{v} \cdot c) = k_{sc} c \tag{17}$$

where $k_{sc} = 2.03 \cdot 10^{-7} m/s$ [8], [12]

No flux boundary condition at all other external boundaries (TDS BC3, Figures 2C & 3) [8], [12]:

$$\nabla \mathrm{c} = 0 \tag{18}$$

Boundary Conditions (Internal)
Flux continuity at all internal boundaries unless otherwise specified.

Initial Condition
All sub-domains except hydrogel ring: Concentration of Ofloxacin=0.
Hydrogel ring: $Concentration = 1.726 \cdot 10^{7} mg/m^3$ (see Appendix 13.6 for derivation)

7 Results

We built a computational model using the input parameters, physics, boundary conditions and initial conditions listed above. All property values were sourced from research literature (either actual values or close substitutes). To shorten computation time, we ran three separate studies in this order: (1) Conjugated stationary study of heat transfer (entire eye) and laminar flow (aqueous humor), (2) Stationary study of Darcy's flow through porous medium (vitreous, retina, choroid, sclera), (3) Time-dependent study of transport of a diluted species (entire eye).

7.1 Heat Transfer and Laminar Flow

We successfully obtained plots of steady-state temperature profile (Figure 4), velocity profile (Figure 5) and pressure distribution (not shown) that agree with results from literature [8], [11].

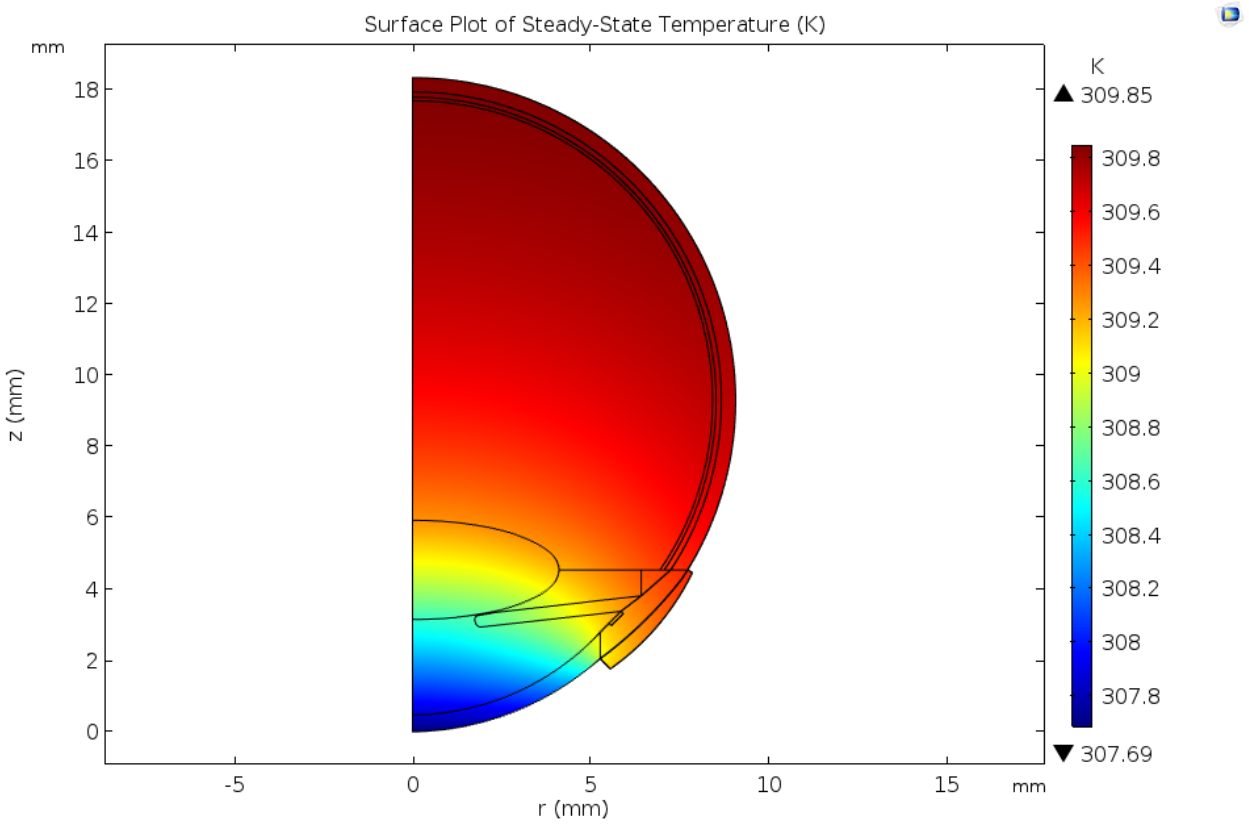

Figure 4. Surface Plot of Steady-State Temperature (K). Temperatures increase steadily from the surface of the eyeball (dark blue) to the back of the eye (dark red). The temperature profile that we have obtained here is in good agreement with the results from other research [8], [11].

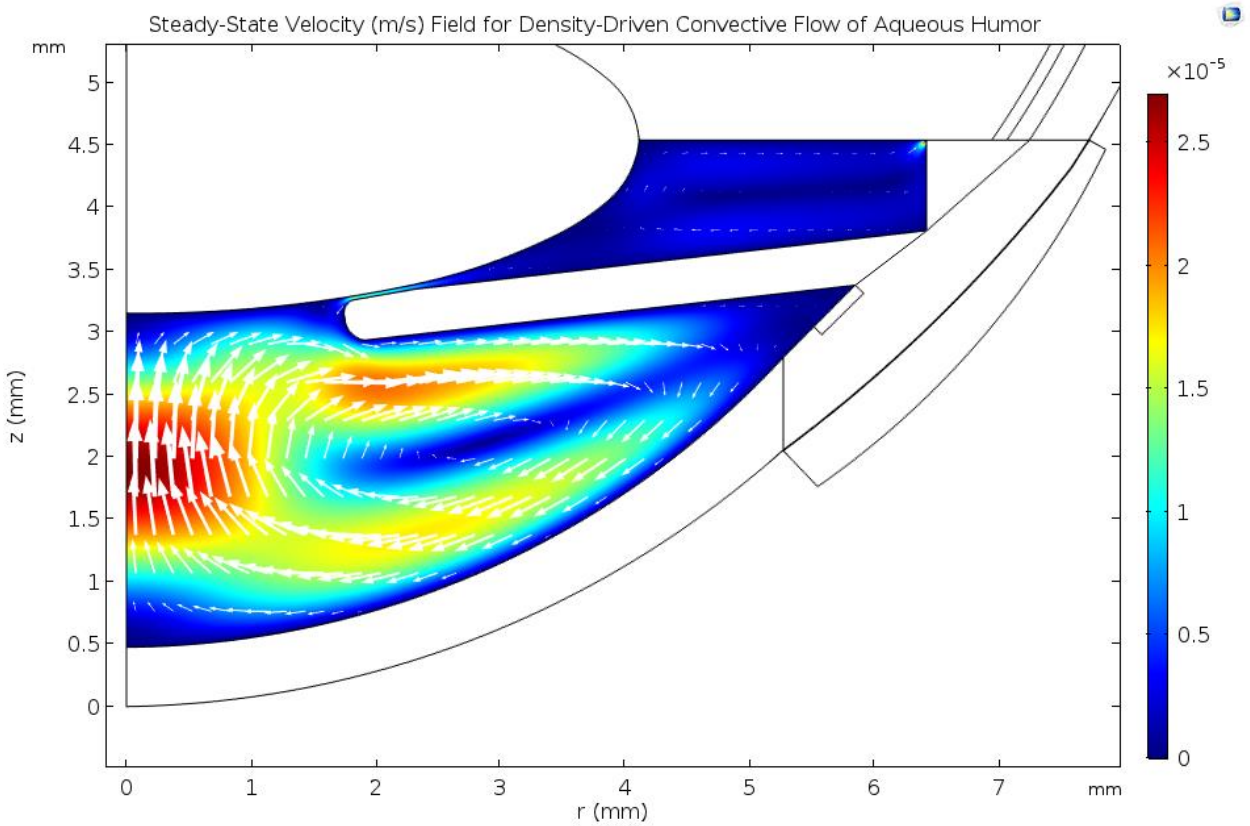

Figure 5. Steady-State Velocity (m/s) Field for Density-Driven Convective Flow of Aqueous Humor. The plot above depicts spatially-varying fluid velocities of aqueous humor in the anterior and posterior chambers, driven by spatially-varying, temperature-dependent density. The plot is in excellent agreement with results obtained in other ocular pharmacokinetics computational models [8], [11].

7.2 Darcy's Flow

Using the Darcy's Flow equation, we solved for fluid velocity in the posterior region of the eye. Figure 6 depicts the combined steady-state velocity profiles of aqueous humor flow in both the anterior and posterior regions.

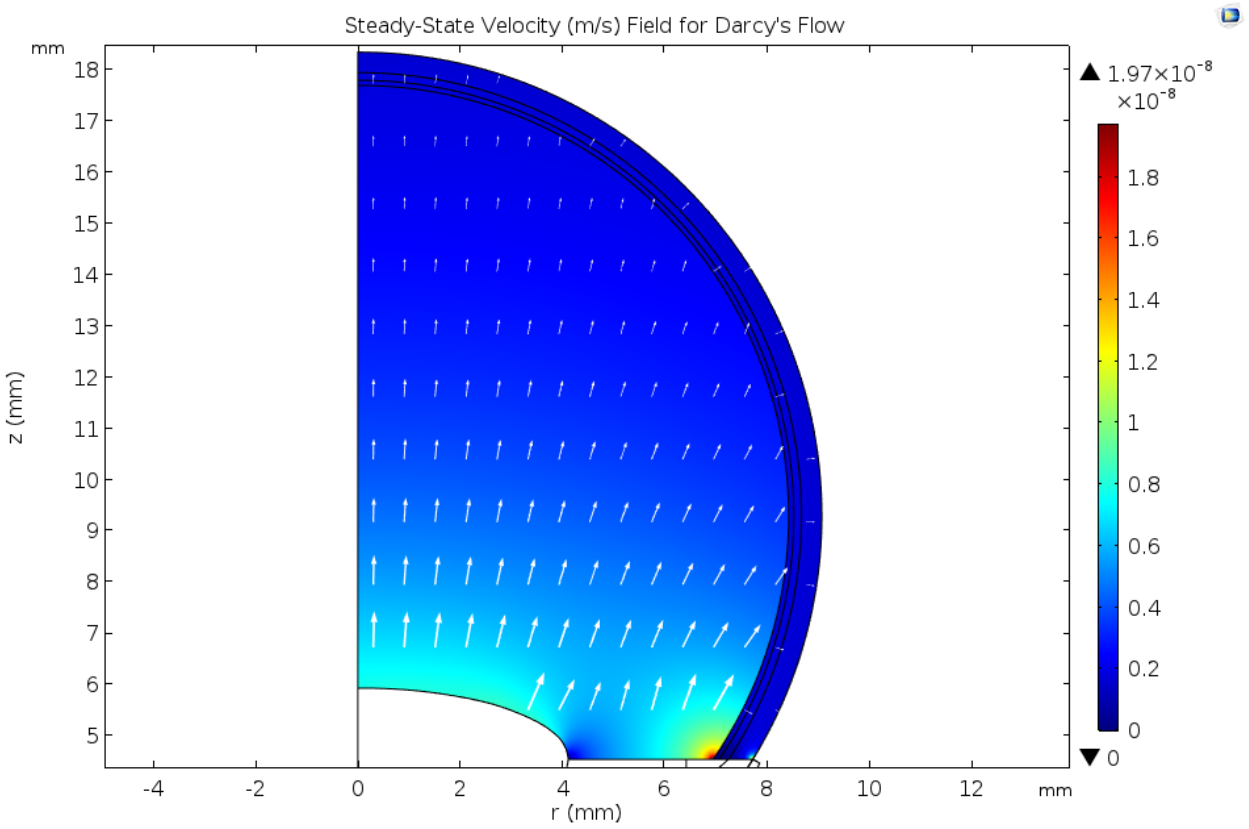

Figure 6. Steady-State Velocity (m/s) Field for Darcy's Flow. The plot above depicts spatially-varying fluid velocities of aqueous humor in the vitreous. Lengths of arrows in the arrow surface plot are proportional to fluid velocity at respective points, i.e. fluid velocity decreases as aqueous humor flows through the vitreous, retina, choroid and sclera.

7.3 Transport of a Diluted Species

Using the velocity profiles developed for buoyancy-driven flow (anterior and posterior chambers) and Darcy's flow (vitreous, retina, choroid, sclera), we solved for the concentration profile of Ofloxacin in the eye. We found that while Ofloxacin diffuses much more quickly to the anterior region than the posterior region, Ofloxacin concentrations do successfully accumulate to therapeutic levels in the posterior tissues during the simulated ten-hour treatment period (Figures 7,8). Please see Appendix Section 13.7 for concentration surface plots at additional time points.

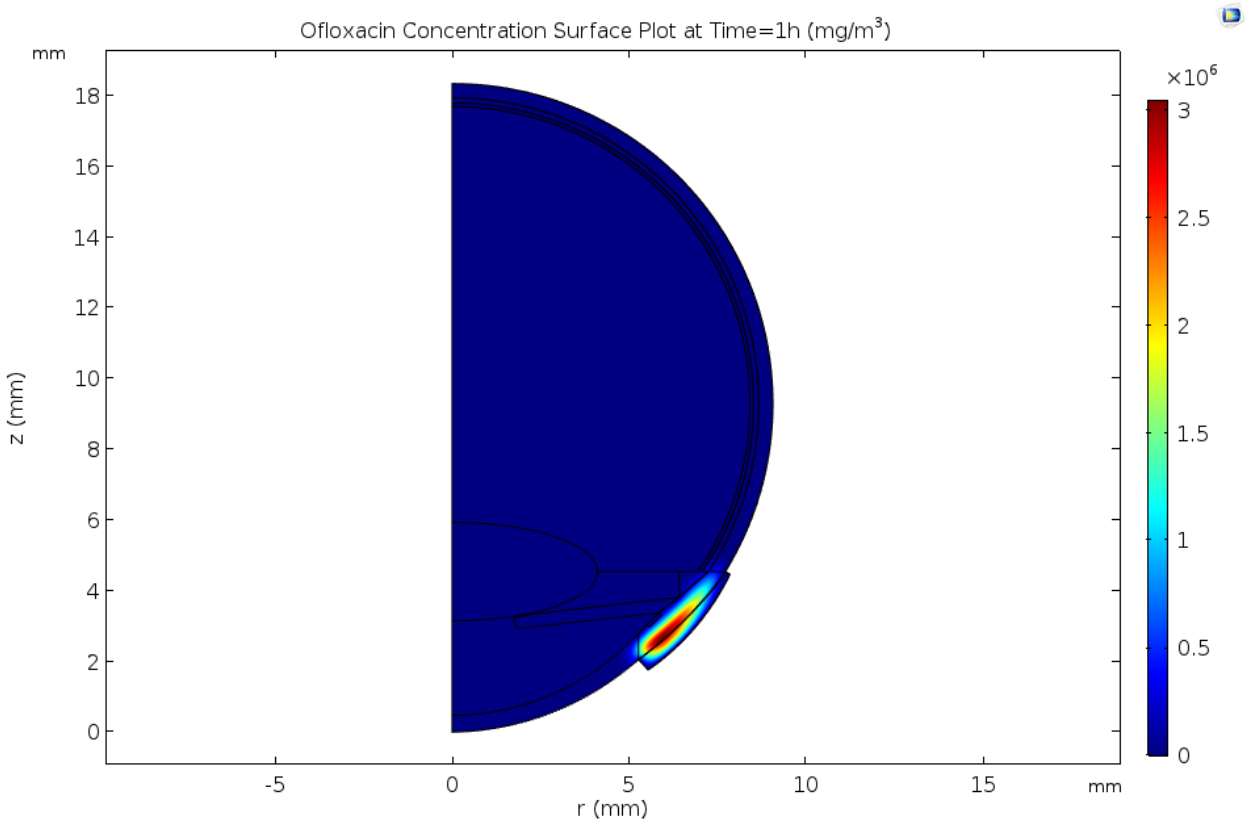

Figure 7. Ofloxacin Concentration Surface Plot at Time=1h (mg/m^3). At time=1h after initial placement of the hydrogel ring, we observe that a considerable portion of the drug has diffused out of the hydrogel ring into the eye. Most of the released drug remains concentrated within the bulbar conjunctiva and the adjacent scleral region.

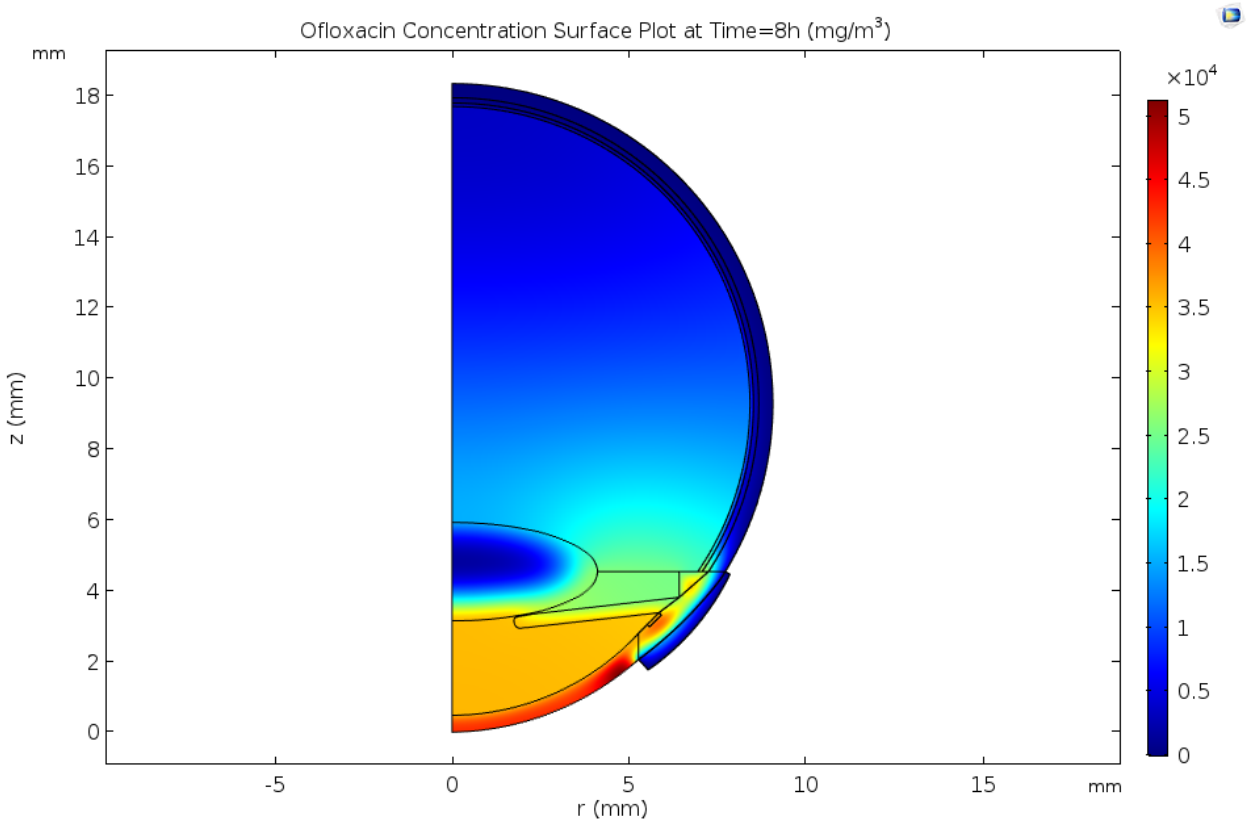

Figure 8. Ofloxacin Concentration Surface Plot at Time-8h (mg/m^3). Compared to Figure 7, concentration in the bulbar conjunctiva (red region) has decreased dramatically. More drug has diffused into other sub-domains and regions of the eye.

8 Mesh Convergence

To minimize spatial discretization error in our model, we performed mesh convergence analysis to determine the smallest possible maximum mesh element size, below which the solution is no longer mesh-dependent (i.e. no significant change to solution with an increase in the number of mesh elements).

We ran our model for a large range of maximum mesh element sizes (from 0.0115mm to 0.5mm) and graphed on the same plot the concentration of Ofloxacin at time=1h along a pre-selected line that passes through points $(0, 2.5)$ and $(6.445, 2.5)$ for all mesh sizes. Figure 9 shows a sub-section of the plot for which there is greatest divergence between the individual data series.

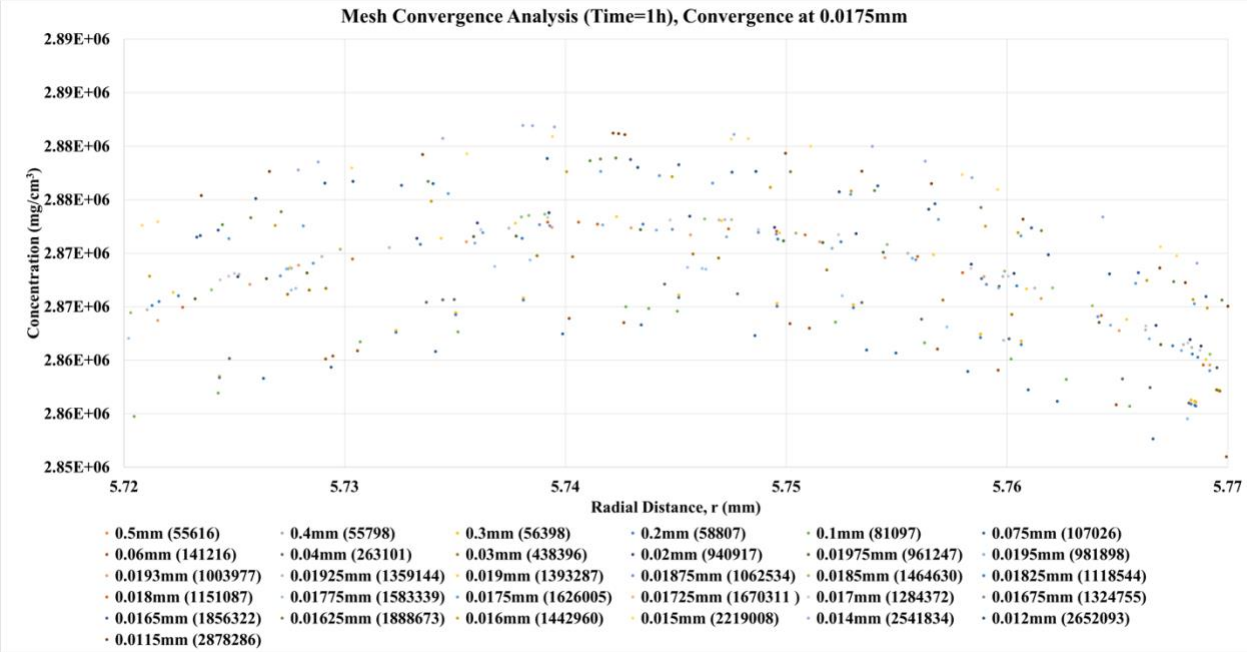

Figure 9. Mesh Convergence Analysis (Time=1h), Convergence at 0.0175mm. The number in parentheses indicates the total number of triangular mesh elements in the mesh corresponding to the specific maximum mesh element size. For each maximum mesh element size, we plotted Ofloxacin concentration along a 2D Cut-Line (from (0, 2.5) to (6.445, 2.5)). This plot can be divided into three broad bands: the smallest mesh sizes (0.0115mm-0.0175mm) form the topmost band, intermediate mesh sizes (0.01775mm-0.03mm) form the middle band, the largest mesh sizes (0.04mm-0.5mm) form the bottom band. Figure 9 is reproduced in Appendix 13.9 in full-page size for greater clarity.

We observe that the plot of concentrations along the 2D Cut-Line oscillates in the same band for maximum mesh element sizes of 0.0175mm and below (Figure 9), suggesting that mesh convergence has occurred using a mesh with 1626005 triangular elements.

To confirm this result, we performed further mesh convergence analysis by comparing the average Ofloxacin concentration at time=1h in posterior eye tissues (i.e. retina, sclera) for five different meshes: maximum mesh element size=0.014mm (2541834 elements), 0.015mm (2219008 elements), 0.0175mm (1626005 elements), 0.02mm (940917 elements), and 0.5mm (55616 elements). We focused on posterior eye tissues since we are most interested in drug delivery to the posterior segment of the eye from the hydrogel ring device. Figures 10 and 11 show the results of this analysis. As expected, mesh convergence is observed for all three meshes with a number of elements greater than or equal to 1626005 (corresponding to maximum mesh element size=0.0175mm).

All computational results and solutions in this paper, unless otherwise stated, were obtained using a mesh with maximum mesh element size of 0.0175mm (1626005 elements), i.e. point of convergence.

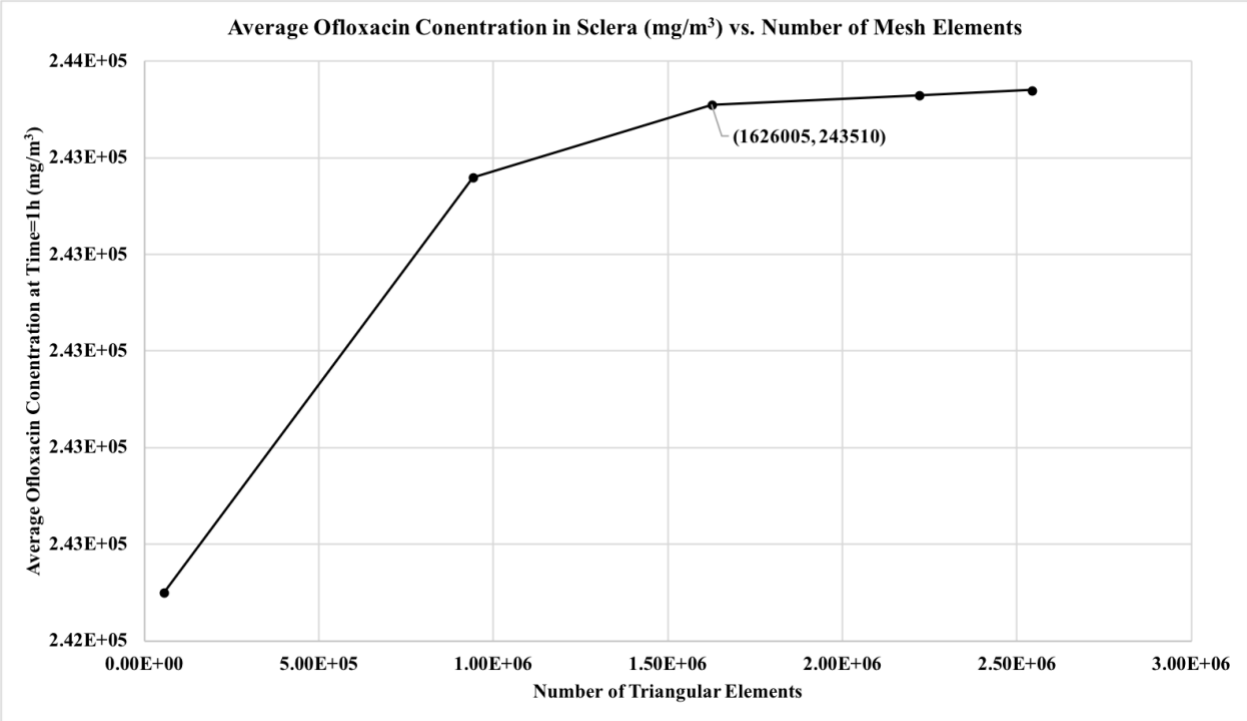

Figure 10. Average Ofloxacin Concentration in Sclera (mg/m^3) vs. Number of Mesh Elements. Mesh convergence is observed for meshes with number of elements greater than or equal to 1626005 (corresponding to maximum mesh element size=0.0175mm).

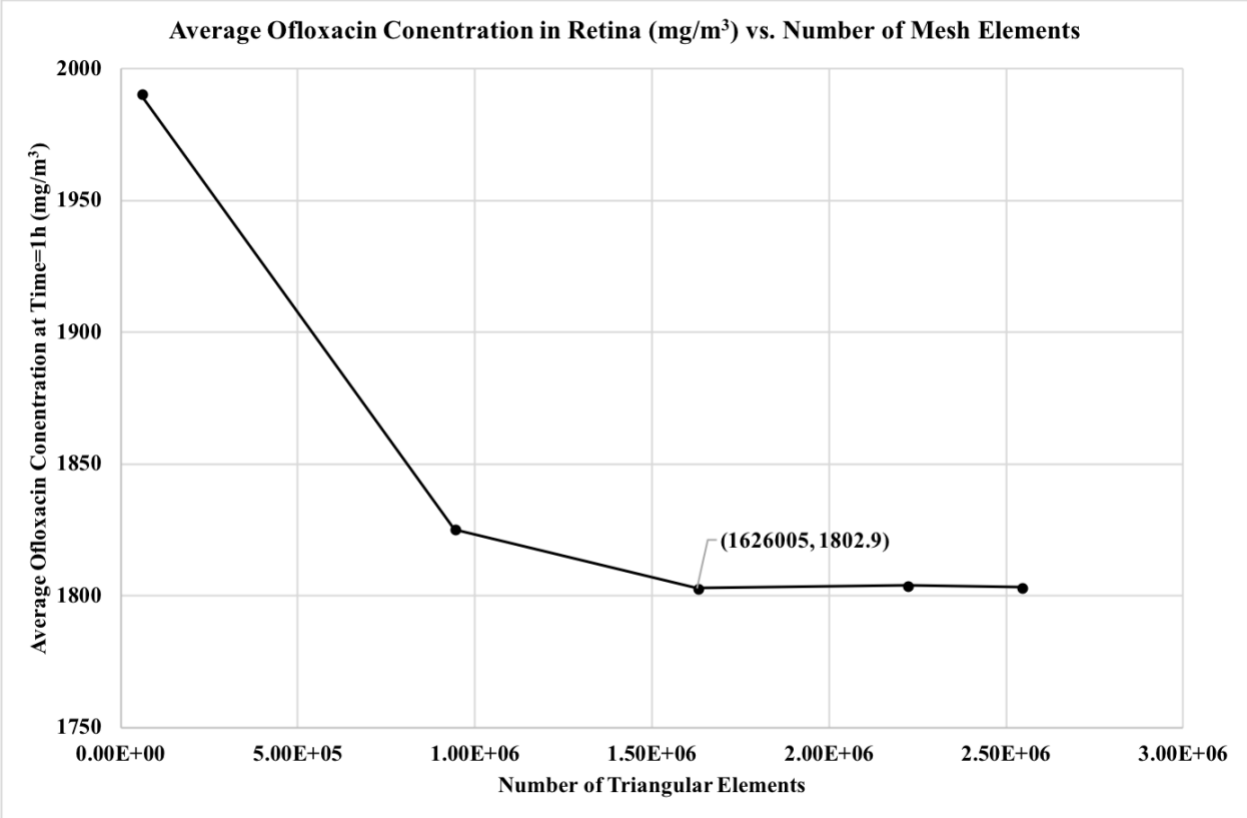

Figure 11. Average Ofloxacin Concentration in Retina (mg/m^3) vs. Number of Mesh Elements. Mesh convergence is observed for meshes with number of triangular elements greater than or equal to 1626005 (corresponding to maximum mesh element size=0.0175mm).

9 Sensitivity Analysis

In our model, we made reasonable assumptions for values of material properties and physical parameters that were unavailable in literature. To determine the effect of potential errors in our assumed values on the computed solution, we performed sensitivity analysis on four main parameters that we believe may contain the most error (i.e. when information for very close substitutes are also unavailable) and/or is closely related to Ofloxacin concentration in sub-domains of interest (i.e. the retina and cornea): (1) Ofloxacin diffusivity in hydrogel ring, (2) Ofloxacin diffusivity in retina, (3) specific heat capacity of hydrogel, and (4) thermal conductivity of hydrogel. We varied these four parameters by $\pm 10\%$ and $\pm 25\%$ and calculated the changes in computational results of interest (i.e. average Ofloxacin concentration in the retina and in the cornea, at times t=1h and t=8h).

Sensitivity analysis revealed that these results of interest are highly sensitive to changes in the diffusivity of Ofloxacin in the hydrogel ring (Figure 12). This result is unsurprising, given that Ofloxacin diffusivity in the hydrogel directly governs the rate of release of Ofloxacin into ocular tissues. Average Ofloxacin concentrations in the retina and cornea at both time points (t=1h and t=8h) are inversely related to Ofloxacin diffusivity in the hydrogel (Figure 12). A possible explanation for this relationship is that as Ofloxacin diffusivity in the hydrogel increases, more drug is lost to blood circulation via the exposed external boundary of the hydrogel ring. Consequently, less of the drug that was initially loaded into the hydrogel actually enters the ocular tissues (see Section 6.4).

Additional analysis showed that while changes in Ofloxacin diffusivity in the retina produced corresponding changes in average Ofloxacin concentration in the retina at both time points, the average concentration of Ofloxacin in the cornea is largely insensitive to these changes (Figure 13). This result may suggest that drug transport in the anterior region of the eye is largely unaffected by changes in changes to material properties of the posterior region.

In contrast, we found that changes in both specific heat capacity and thermal conductivity of the hydrogel produced no change in average Ofloxacin concentration in the retina and cornea at both time points.

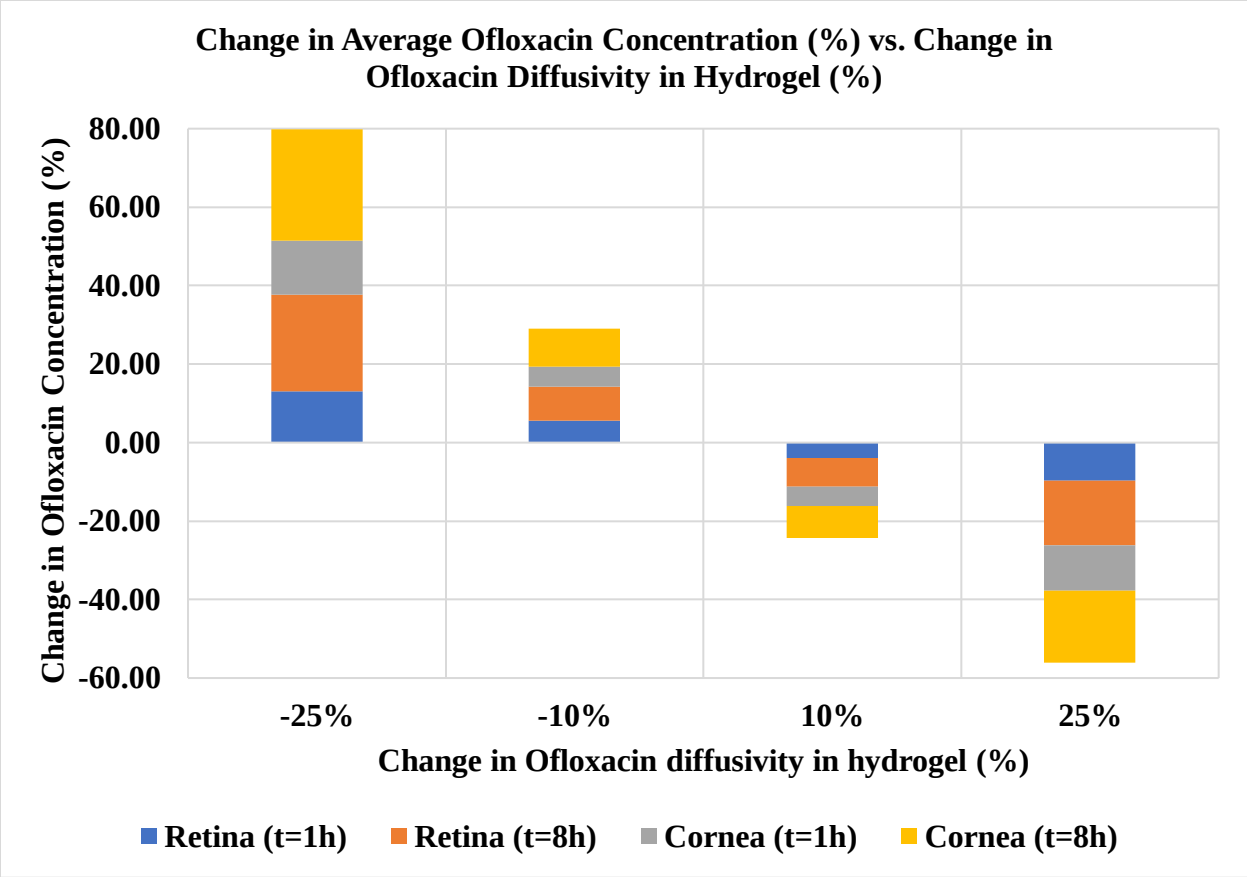

Figure 12. Change in Average Ofloxacin Concentration (%) vs. Change in Ofloxacin Diffusivity in Hydrogel (%). Average Ofloxacin concentrations in both the retina and cornea at both time points (t=1h and t=8h) increase as Ofloxacin diffusivity in the hydrogel decreases, and vice versa. Average Ofloxacin concentrations in the retina and cornea at time t=8h are highly sensitive to changes in Ofloxacin diffusivity in the hydrogel: a -25% change in Ofloxacin diffusivity produces 24.67% and 28.45% increases in average Ofloxacin concentration in the retina and cornea, respectively.

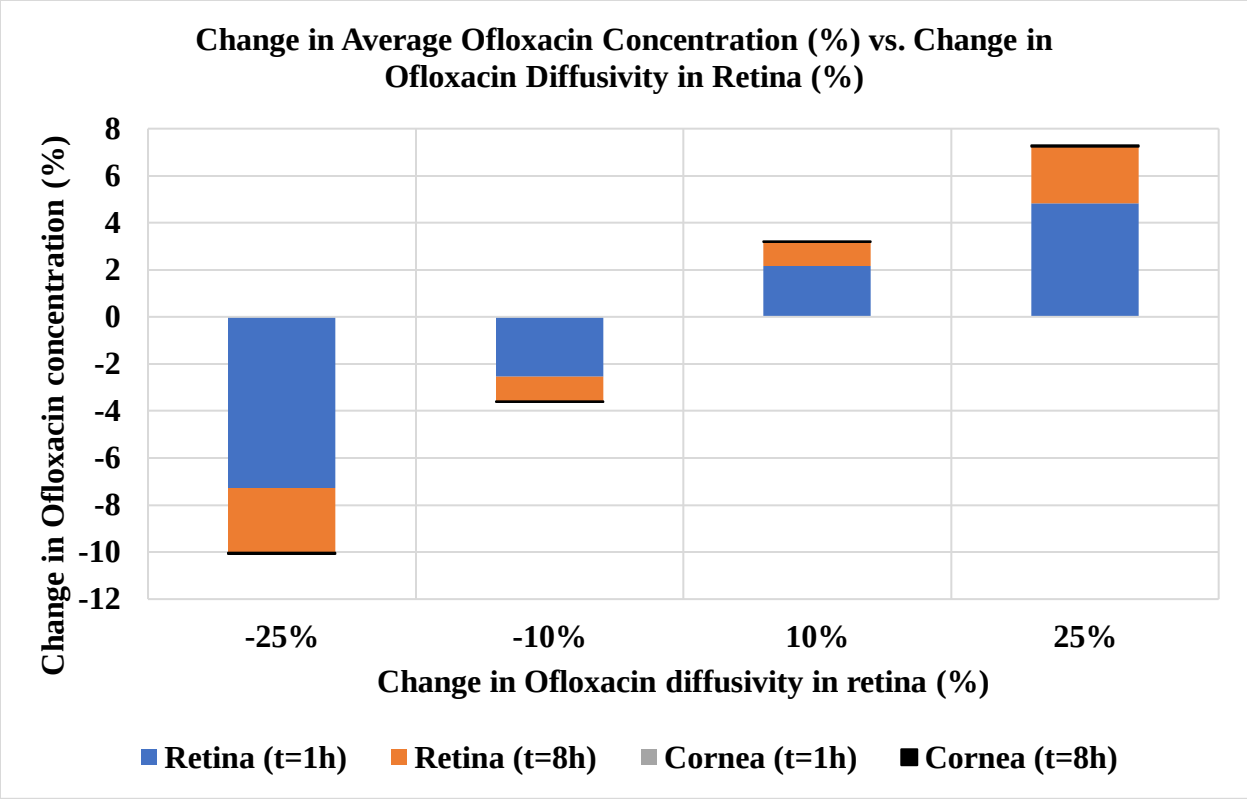

Figure 13. Change in Average Ofloxacin Concentration (%) vs. Change in Ofloxacin Diffusivity in Retina (%). Average Ofloxacin concentration in the retina at both time points (t=1h and t=8h) are highly sensitive (and directly related) to changes in Ofloxacin diffusivity in the retina. In contrast, changes in Ofloxacin diffusivity in the retina produced negligible changes in terms of average Ofloxacin concentration in the cornea.

10 Validation

We validated our computational results by comparing average Ofloxacin concentration in various ocular tissues at time=1h with the experimental data from [6]. From Table 1, we observe that while there is good agreement between computed and experimental Ofloxacin concentration in the combined retina + choroid tissues, there are significant differences between experimental and computational results for other ocular tissues, especially in the bulbar conjunctiva and sclera (Table 1). Given that the experimental data from [6] is derived from rabbits while our computational study is based on a human eye model, we suspect that the large discrepancies in the spatial distribution of Ofloxacin concentrations between the computed results and experimental data may be largely attributed to differences in organization and relative sizes of anterior regions of rabbit and human eyes [13].

The above comparison, however, suggests that our model remains useful in modeling drug transport to posterior eye segments, i.e. the retina and choroid, and in predicting accumulated drug levels in posterior eye tissues.

Table 1. Comparison of computational results with experimental data.

	Ofloxacin Concentration (mg/m^3)				
	Cornea	**Bulbar Conjunctiva**	**Sclera**	**Aqueous Humor**	**Retina + Choroid**
[6]	13000 (3.73)	29900 (8.59)	7770 (2.23)	3800 (1.09)	3480 (1)
Group03	63814 (17.0)	1545100 (412)	243510 (65.0)	8364.1 (2.23)	3746.9 (1)

Note: Number in parentheses indicates ratio of Ofloxacin concentration in a particular ocular tissue relative to that in the retina + choroid (combined).

To provide further validation for our computational model, we compared the cumulative amount of Ofloxacin released from the hydrogel over time as obtained in [6], with that calculated using our model (Figure 14). A direct comparison between our model results and data from [6] reveals that the cumulative drug release profile obtained through our model is of the same general shape as that obtained experimentally (Figure 14, blue vs. red plots), but the profile obtained via modeling is much steeper (Figure 14). Given the high sensitivity of the computed solution to changes in Ofloxacin diffusivity in the hydrogel (see Section 8), we hypothesized that the difference in experimental and computed drug release profiles may be due to an overestimation in the value for Ofloxacin diffusivity in the hydrogel, in our model.

This hypothesis is supported by the green plot in Figure 14, obtained by decreasing Ofloxacin diffusivity in the hydrogel by one order of magnitude from the original value used. Compared to the original red plot, the green plot provides a much better fit to the experimentally-derived drug

release profile (Figure 14). Here, we note that our model is based on several approximations of the thermal and drug transport properties of the hydrogel ring (due to unavailability of precise data and detailed specifications from literature). We thus believe that the fit between our model and experimental data can be further improved with further finetuning of assumed physical parameter values and material properties.

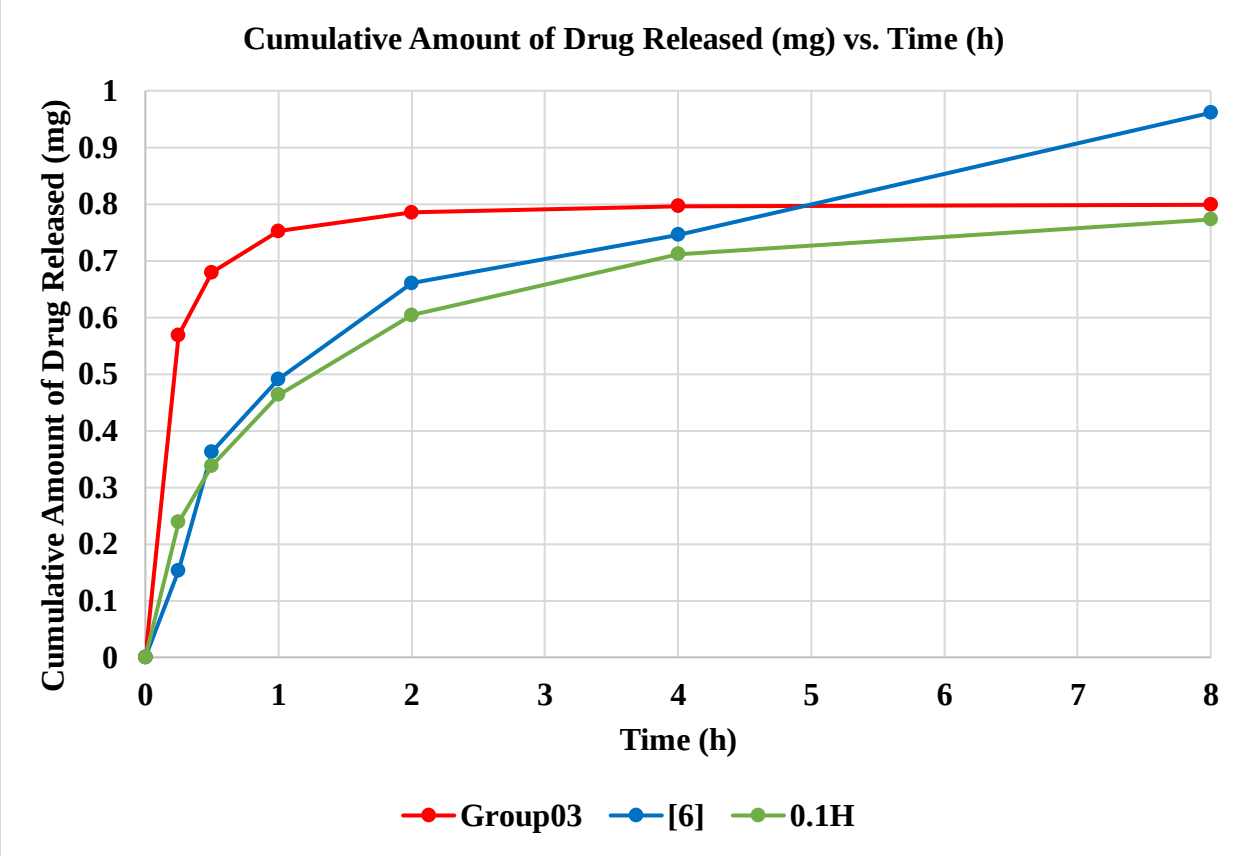

Figure 14. Cumulative Amount of Drug Released (mg) vs. Time (h). This figure compares the computed drug release profile from times t=0h to t=8h with that based on the data in [6]. There is a sharp burst release at very early time points (t<0.5h), followed by a steady release at subsequent time points. The green plot is obtained by decreasing Ofloxacin diffusivity in the hydrogel by one order of magnitude (from the value used to obtain the red plot).

11 Optimization

To demonstrate the potential of the computational model for design and optimization studies, we performed a simple optimization analysis to determine the optimal hydrogel ring design for the treatment of ocular infections caused by various species of bacteria: *Escherichia coli*, *Staphylococcus aureus*, and *Streptococcus pneumoniae*. We optimized two design parameters: (1) initial mass of Ofloxacin loaded into the hydrogel ring (IM), and (2) Ofloxacin diffusivity in the hydrogel (HD).

The ideal hydrogel ring design would be able to deliver a sustained release of Ofloxacin, as well as maintain Ofloxacin concentrations in the cornea and the retina within the therapeutic window for as long as possible. The upper bound of the therapeutic window is the Ofloxacin concentration that is considered toxic for a specific ocular tissue, and the lower bound is the Minimum Inhibitory Concentration for 90% of isolates of a particular bacterial species (i.e. MIC_{90}) [14].

We developed an objective function, which can be used to evaluate the therapeutic effectiveness of various combinations of IM and HD (Equation 19). The best combination of IM and HD is one that maximizes the value of the objective function value, J. Further information on the sub-functions F_C and F_R can be found in the Appendix 13.10.

$$J = \sum_{i=1}^{12244} F_C(c_i) + \sum_{j=1}^{8405} F_R\left(c_j\right) \tag{19}$$

We ran the model for 16 different pairs of IM values and HD values (i.e. 4 different values each). From our results, we found that for constant values of MIC_{90} and IM, J decreases as HD decreases (Appendix 13.10). We thus selected cases 1, 5, 9, and 13 (of which the value of HD is the highest of the four values tested) for further analysis (Appendix 13.10).

We found that the combination of $HD = 3.11 \cdot 10^{-9} m^2/s$ and $IM = 3mg$ is most ideal for the treatment of both *E. coli* (Figure 15) and *S. aureus* infections (Figure 16). We were not able to obtain a satisfactorily optimized combination of HD and IM values for the treatment of *S. pneumoniae* infections (Figure 17)—it is possible that the optimal combination may lie outside the relatively narrow range that we tested for this sample calculation.

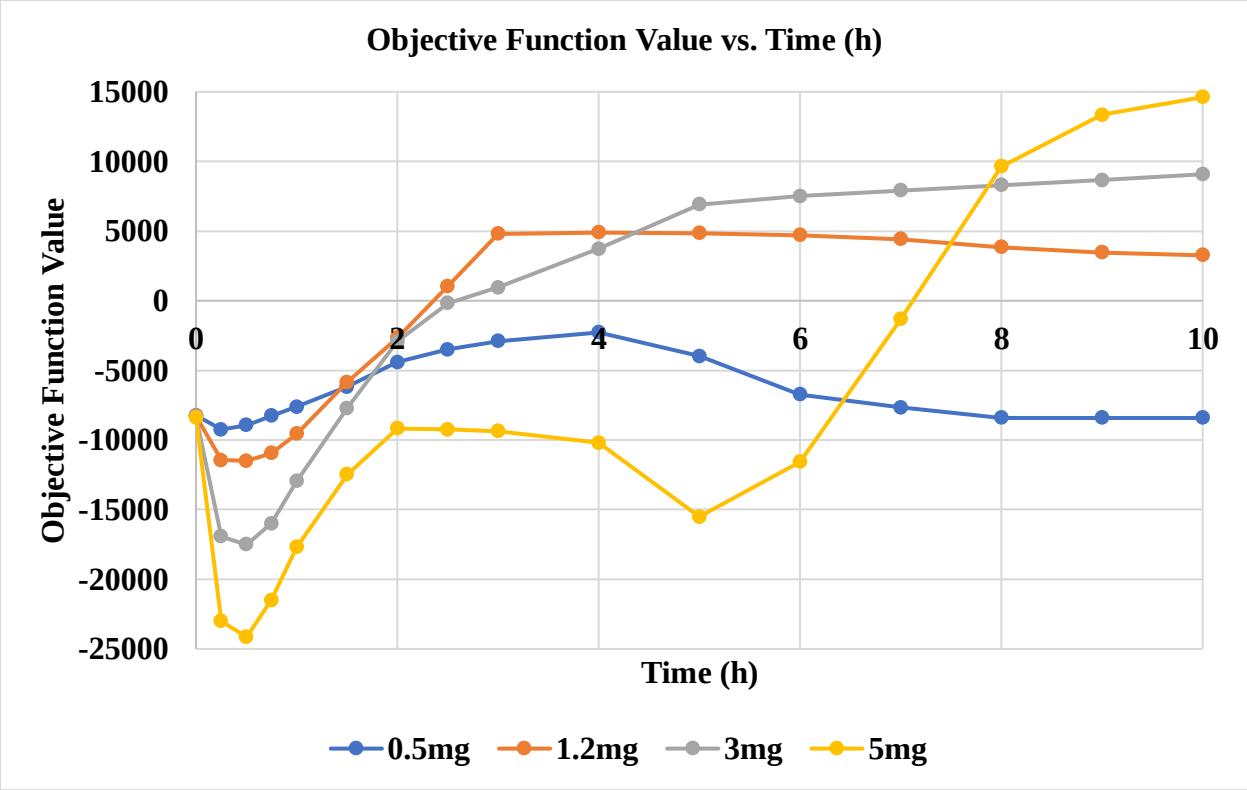

Figure 15. Objective Function Value vs. Time (h). This plot is for $MIC_{90} = 250mg/m^3$, i.e. treatment of *E. coli*. At earlier times, objective function values are very negative (i.e. far from therapeutic goal) because very little drug has diffused to the cornea and retina. At later times, the increase in objective function value due to the accumulation of drug in the retina may be offset by the decrease in objective function value due to an excessive accumulation in the cornea (past toxic threshold). $IM = 3mg$ appears to provide a balanced and most-ideal therapeutic outcome: it yields the highest/second-highest objective function value for 80% of the treatment time.

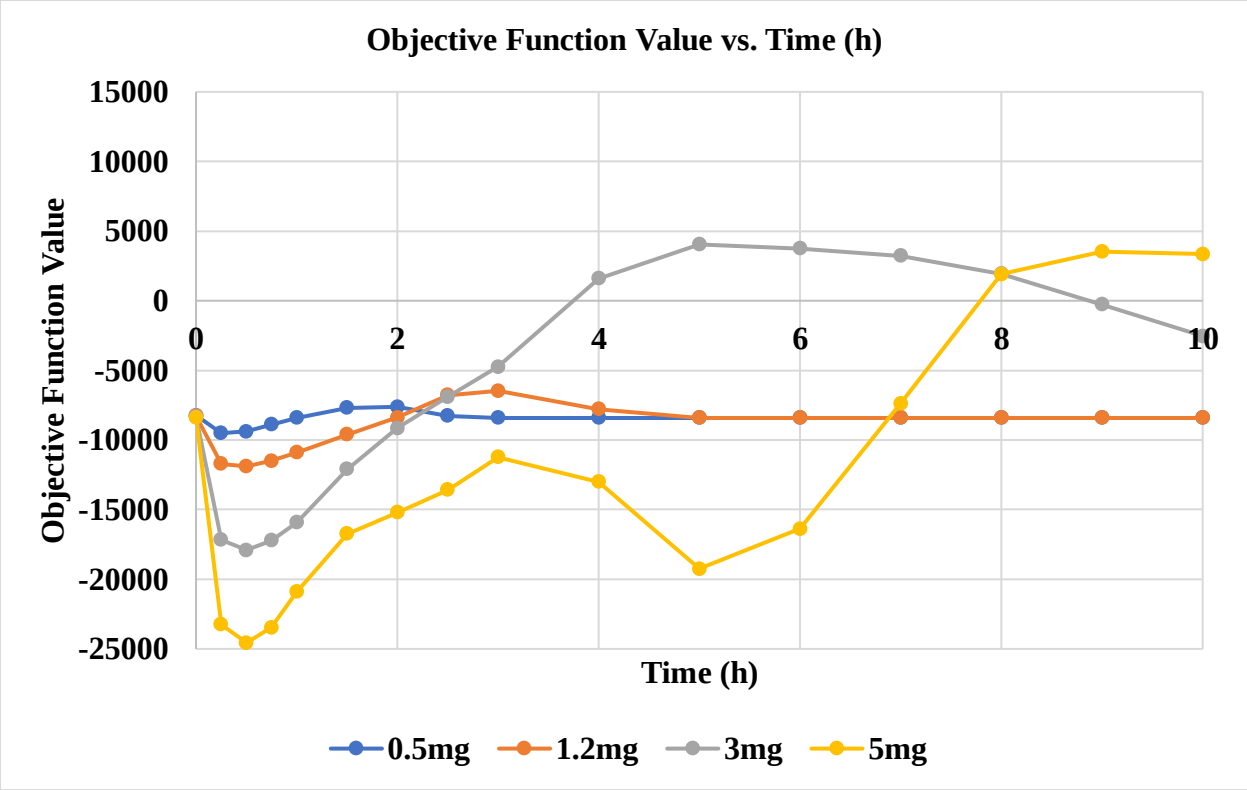

Figure 16. Objective Function Value vs. Time (h). This plot is for $MIC_{90} = 1000mg/m^3$, i.e. treatment of *S. aureus.* At earlier times, objective function values are very negative (i.e. far from therapeutic goal) because very little drug has diffused to the cornea and retina. At later times, the increase in objective function value due to the accumulation of drug in the retina may be offset by the decrease in objective function value due to an excessive accumulation in the cornea (past toxic threshold). $IM = 3mg$ appears to provide a balanced and most-ideal therapeutic outcome: it yields the highest/second-highest objective function value for approximately 80% of the treatment time.

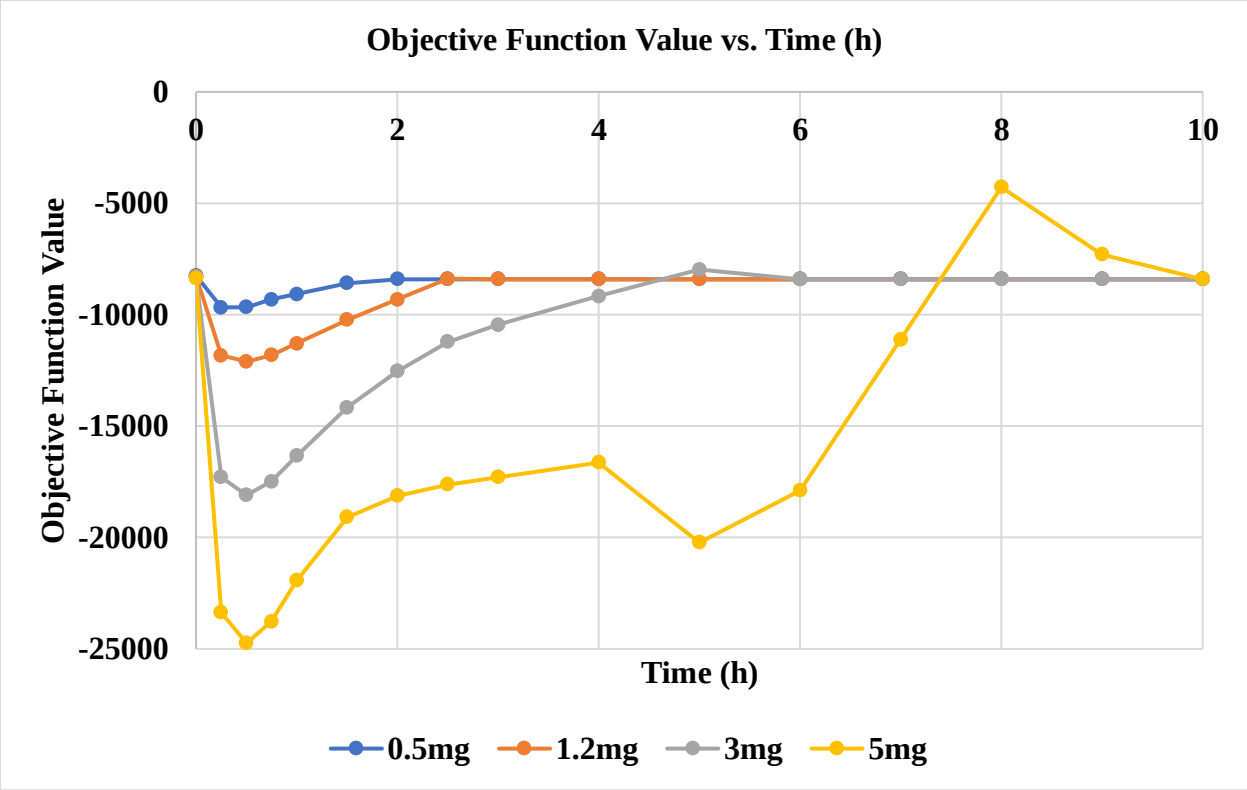

Figure 17. Objective Function Value vs. Time (h). This plot is for $MIC_{90} = 2000 mg/m^3$, i.e. treatment of *S. pneumoniae.* At earlier times, objective function values are very negative (i.e. far from therapeutic goal) because very little drug has diffused to the cornea and retina. At later times, the increase in objective function value due to the accumulation of drug in the retina may be offset by the decrease in objective function value due to an excessive accumulation in the cornea (past toxic threshold). There is no clear optimized IM for $MIC_{90} = 2000 mg/m^3$ since the objective function values are very negative for all IM values tested.

12 Conclusion and Design Recommendations

We have completed a computational study of a hydrogel ring device for ocular drug delivery and achieved the design objectives of our study. Using our computational model, we determined the spatial and temporal drug distribution in ocular tissues during treatment with the hydrogel ring device. Our modeling results validate the therapeutic potential of the hydrogel ring in the treatment of posterior segment ocular disorders. We have also completed a preliminary optimization study to optimize the hydrogel ring design parameters for the therapeutic treatment of three different types of bacterial infections.

Further studies on the hydrogel ring device may use our computational model to determine the compatibility of the hydrogel ring with other ocular pharmaceuticals, as well as optimize a wider range of design parameters, e.g. physical dimensions of the hydrogel ring. Ultimately, modeling results must also be corroborated by additional experimental data to support the use of the hydrogel ring device in clinical applications.

Future computational work on ocular pharmacokinetics in general may finetune our model to account for more processes associated with drug transport, including (but not limited to) lacrimal tear drainage [9], vitreous motion due to eye rotations [15], and drug loss due to active pumping by the retinal pigment epithelium and retinal capillaries [12]. Future studies may also consider adapting our 2D-axisymmetric model into a 3D model in order to model the case in which the patient is standing upright (i.e. not lying down, as assumed in our model). A 3D model is necessary for this scenario, since the axis about which the gravitational force vector is rotationally symmetric is not the same as the axis about which eye geometry is rotationally symmetric.

13 Appendix

13.1 Geometry and Physical Dimensions

As we were unable to obtain a satisfactory human eye computational model from research literature, we constructed an anatomically-accurate computational geometry based on physical dimensions obtained from various sources [6], [9], [12], [16] (Figure A1).

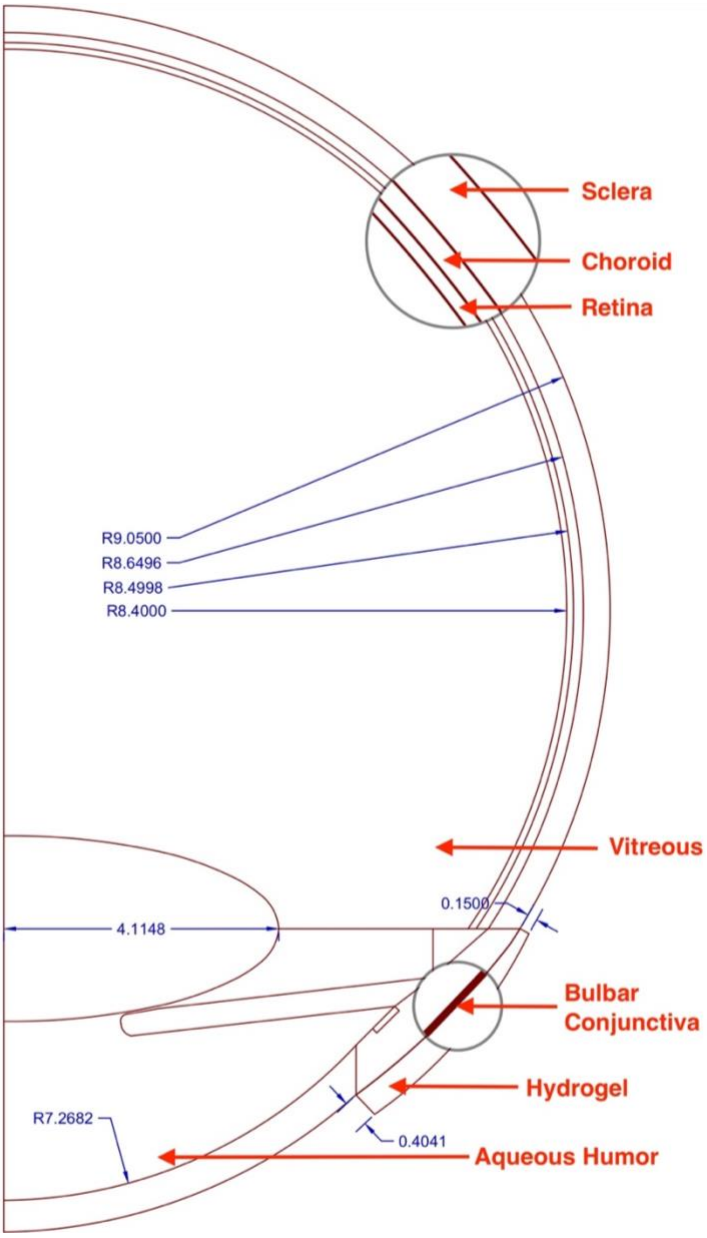

Figure A1. Labeled Computational Geometry and Physical Dimensions. We created the computational geometry using SolidWorks® (Dassault Systèmes, Vélizy-Villacoublay, France), with all physical dimensions (in mm) derived from literature [6], [9], [12], [16].

13.2 Input Parameters for Heat Transfer

Table 2. Thermal Properties Specified for Computational Sub-Domains.

Sub-Domain	**k** $\left(\frac{\mathbf{W}}{\mathbf{m \cdot k}}\right)$	**c** $\left(\frac{\mathbf{J}}{\mathbf{kg \cdot K}}\right)$	**ρ** $\left(\frac{\mathbf{kg}}{\mathbf{m^3}}\right)$	**u** $\left(\frac{\mathbf{m}}{\mathbf{s}}\right)$	**Source**
Cornea	0.58	4178	1050	0	[8]
Vitreous	0.603	4178	1000	0	[8]
Sclera	1.0042	3180	1100	0	[8]
Retina*	1.0042	3180	1100		
Choroid*	1.0042	3180	1100		
Bulbar Conjunctiva*	1.0042	3180	1100		
Iris	1.0042	3180	1100	0	[8]
Aqueous Humor (fluid)	0.58	3997	$\rho(T)$ (coupled in laminar flow)	u (solved in laminar flow)	[8]
Ciliary Body	1.0042	3180	1100	0	[8]
Lens	0.4	3000	1050	0	[8]
Trabecular Meshwork	1.0042	3180	1100	0	[8]
Hydrogel	0.5^	1150#	1403.83404	0	**k:** [17] **c:** [18] **ρ:** [6]

*assumed to have the same input parameters as the sclera

^approximated based on range of thermal conductivities for polyacrylamide hydrogels

#approximated to be the same as the heat conductivity of water in a poly(methy1methacrylate) hydrogel membrane

13.3 Input Parameters for Laminar Flow

Table 3. Input Parameters Specified in Computational Model for Laminar Flow Physics.

Input Parameter	Value	Source
ρ_0	996 $\left[\frac{kg}{m^3}\right]$	[8]
μ	0.00074 $[Pa \cdot s]$	[8]
β	0.000337 $\left[\frac{1}{K}\right]$	[8]
g	9.81 $\left[\frac{m}{s^2}\right]$	[8]
T_{ref}	307 $[K]$	[8]
Q_{ah}	2.4 $\left[\frac{\mu L}{min}\right]$	[8]
A_{cb}	34.04 $[mm^2]$	[8]

13.4 Input Parameters for Darcy's Flow

Table 4. Input Parameters Specified in Computational Model for Darcy's Flow Physics.

Sub-Domain	$\frac{\mathbf{K}}{\boldsymbol{\mu}}$ $(\mathbf{cm^2/Pa \cdot s})$	$\boldsymbol{\varepsilon}$	Source
Vitreous	$8.4 \cdot 10^{-7}$	0.5*	[12]
Retina	$2.36 \cdot 10^{-11}$	0.5*	[12]
Choroid	$1.5 \cdot 10^{-11}$	0.5*	[12]
Sclera	$1.5 \cdot 10^{-11}$	0.5*	[12]

*assumed porosity value

13.5 Input Parameters for Transport of a Diluted Species

Table 5. Input Parameters Specified in Computational Model for Species Transport.

Sub-Domain	Diffusion Coefficient for Ofloxacin $(\mathbf{cm^2/s})$	Source
Cornea	$1 \cdot 10^{-7}$	[7]
Vitreous	$1 \cdot 10^{-5}$	[7]
Sclera	$1 \cdot 10^{-7}$	[7]
Bulbar Conjunctiva*	$1 \cdot 10^{-7}$	
Iris	$1 \cdot 10^{-6}$	[7]
Aqueous Humor	$1 \cdot 10^{-4}$	[7]
Ciliary Body	$1 \cdot 10^{-7}$	[7]
Lens	$1 \cdot 10^{-7}$	[7]
Trabecular Meshwork	$1 \cdot 10^{-7}$	[7]

Retina^	$1 \cdot 10^{-8}$	
Choroid*	$1 \cdot 10^{-7}$	
Hydrogel#	$3.11 \cdot 10^{-11}$	[19]

*assumed to be the same as the diffusion coefficient in sclera [8]

^assumed to be 0.1 of diffusion coefficient in sclera

#approximated to be the same as that of Levofloxacin (left-sided isomer of Ofloxacin) in 98/2 (w/w) 2-hydroxyethyl methacrylate (HEMA)/ Poly(vinylpyrrolidone) (PVP) hydrogel

Table 6. Domain-Specific Inputs for $\vec{v}$ and k in Transport Equation.

Sub-Domain	$\vec{v}$	**k**	**Source**
Sclera	Darcy Flow (see 6.3)	$\gamma(c_{bl} - c)$, $\gamma = 1.98 \cdot 10^{-5} s^{-1}$, $c_{bl} = 0$	[12]
Choroid	Darcy Flow (see 6.3)	$\gamma(c_{bl} - c)$, $\gamma = 1.98 \cdot 10^{-5} s^{-1}$, $c_{bl} = 0$	[12]
Retina	Darcy Flow (see 6.3)	0	[12]
Vitreous	Darcy Flow (see 6.3)	0	[12]
Bulbar Conjunctiva	0	0	[12]
Lens	0	0	[8]
Cornea	0	0	[8]
Anterior Chamber	Buoyancy Driven Flow (see 6.2)	0	[8]
Posterior Chamber	Buoyancy Driven Flow (see 6.2)	0	[8]
Trabecular Meshwork			
Iris	0	0	[8]
Ciliary Body	0	0	[8]
Hydrogel	0	0	[6]

13.6 Derivation of Initial Concentration of Ofloxacin in Hydrogel Ring

Given in [6]: Hydrogel ring is 38wt% water, total weight of hydrogel ring is 183mg, weight of Ofloxacin loaded into hydrogel ring is $1200\mu g$.

Assume: Density of water is $1 g/cm^3 = 1 g/mL$

$$Volume\ of\ water\ in\ hydrogel\ ring = 0.38 \cdot 183mg = 69.54mg = 69.54 \cdot 10^{-3} mL$$

$$Initial\ concentration\ of\ Ofloxacin\ in\ hydrogel\ ring = \frac{1200 \cdot 10^{-3} mg}{69.54 \cdot 10^{-3} cm^3 \left(\frac{1m^3}{10^6 cm^3}\right)}$$

$$= 17256255.39 mg/m^3$$

13.7 Concentration Surface Plots

The following figures show the concentration surface plots for times t=0h to t=10h (Figures A2, A3).

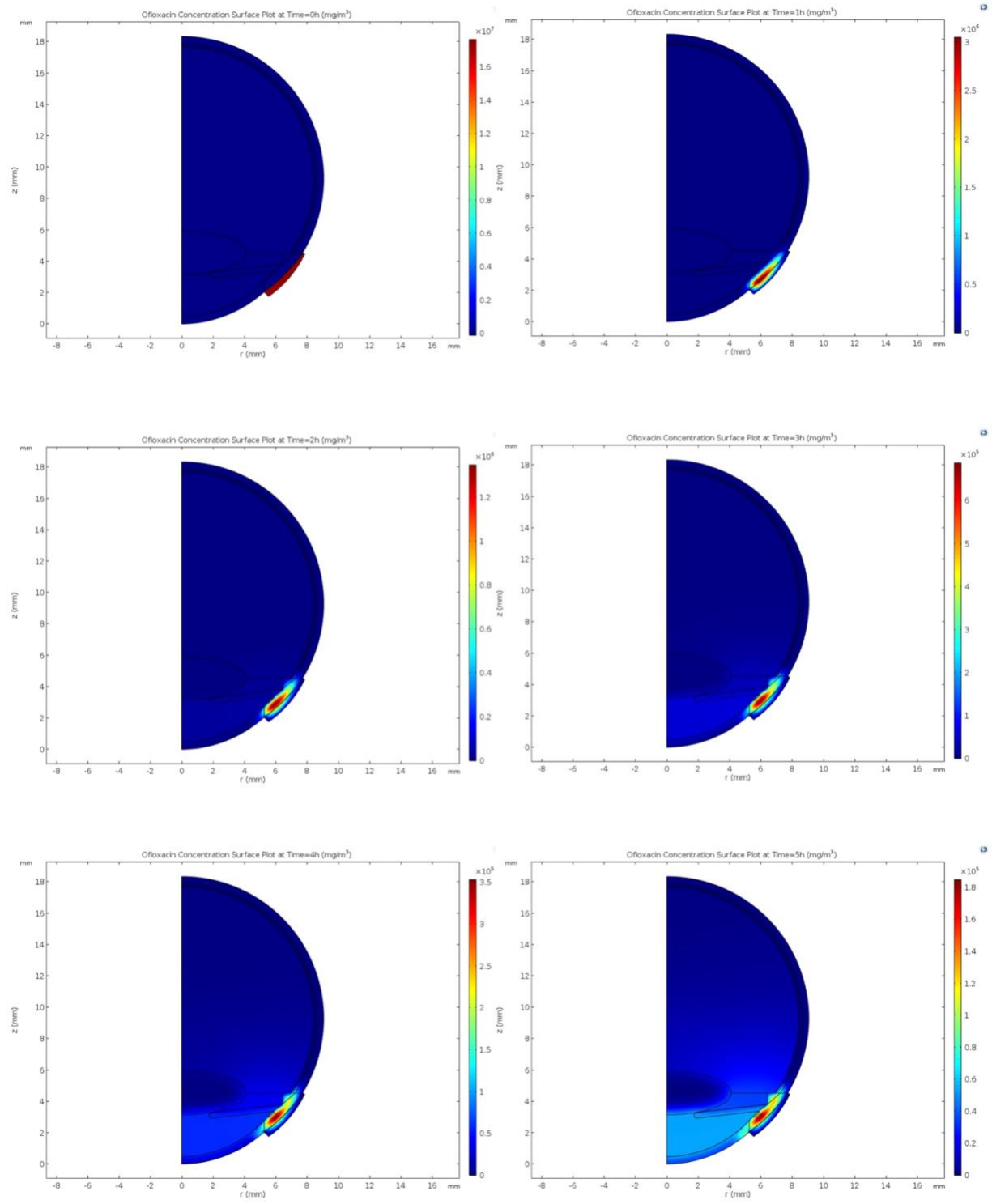

Figure A2. Ofloxacin Concentration Surface Plot at Time=0h to Time=5h (mg/m^3). Ofloxacin diffuses out of the hydrogel and enters the anterior first before diffusing to the posterior region. Most of the drug has diffused out of the hydrogel by time=5h.

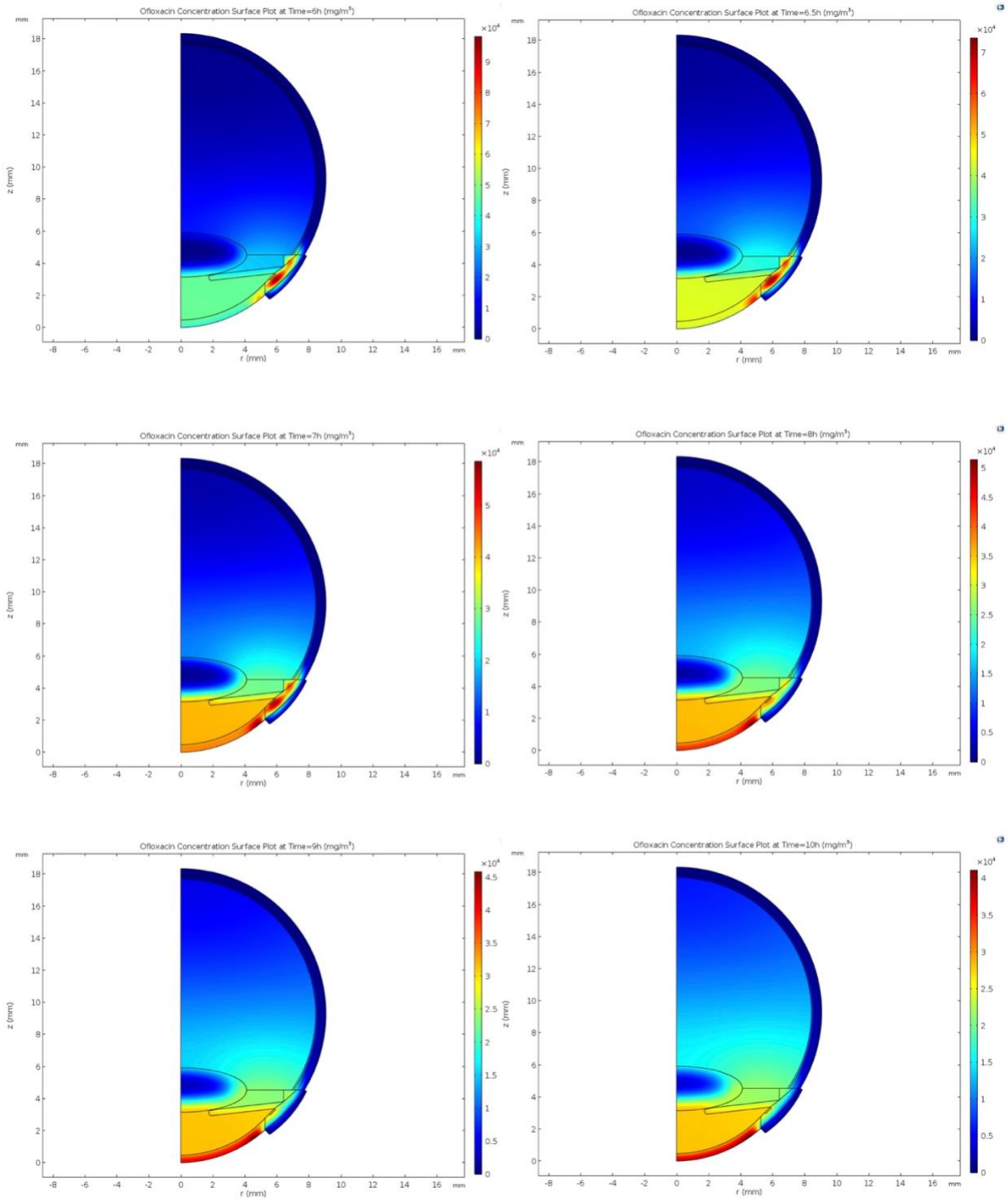

Figure A3. Ofloxacin Concentration Surface Plot at Time=6h to Time=10h (mg/m^3). Ofloxacin begins to accumulate in posterior segment tissues at later times. Ofloxacin concentrations in various sub-domains approach steady-state at time=10h.

13.8 Mesh and Study Statistics

13.8.1 Mesh for Computational Studies (1, 2, 3)

Mesh type: Free triangular
Total number of triangular elements: 1626005
Number of edge elements: 9056
Number of vertex elements: 43
Number of mesh vertices: 814387

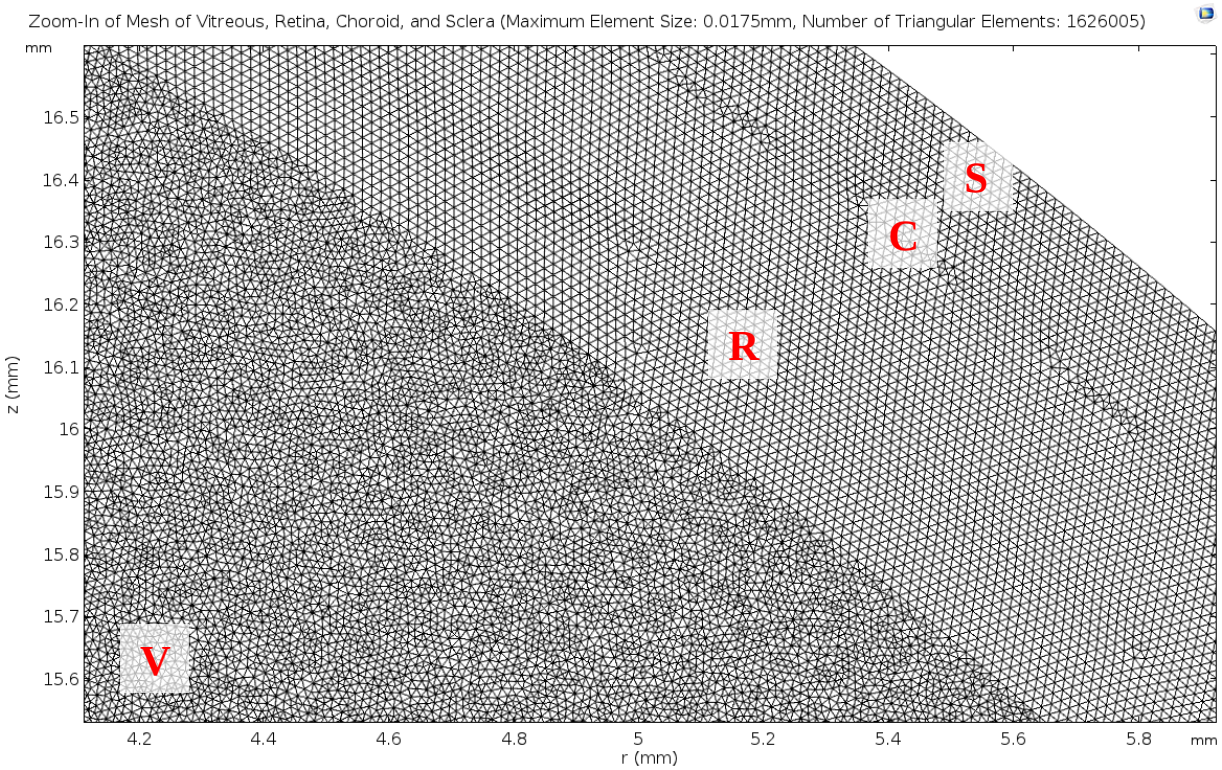

Figure A4. Zoom-in of Mesh of Vitreous, Retina, Choroid, and Sclera. Vitreous (V); retina (R); choroid (C); sclera (S). The maximum mesh element size is 0.0175mm.

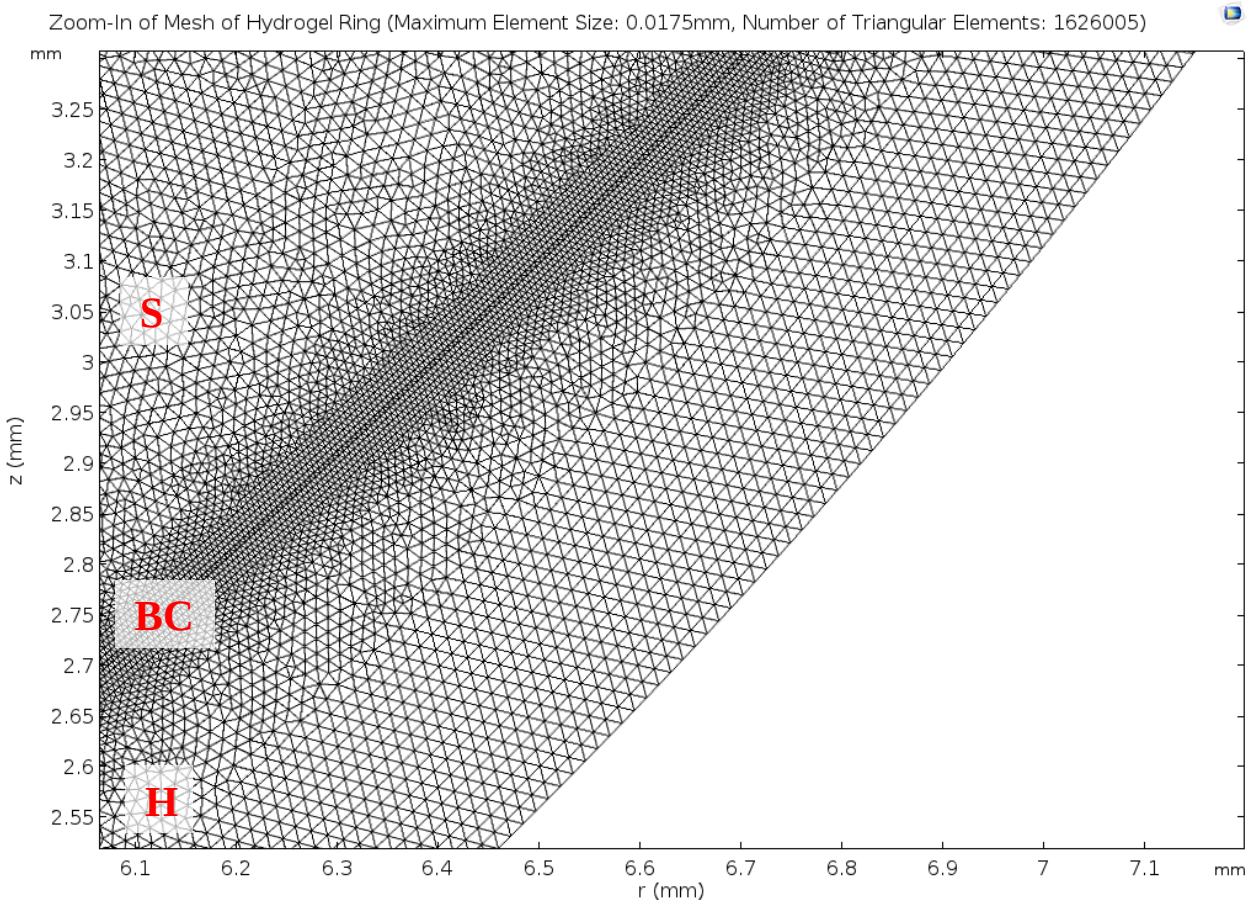

Figure A5. Zoom-In of Mesh of Hydrogel Ring. Hydrogel ring (H); bulbar conjunctiva (BC); sclera (S). The maximum mesh element size is 0.0175mm.

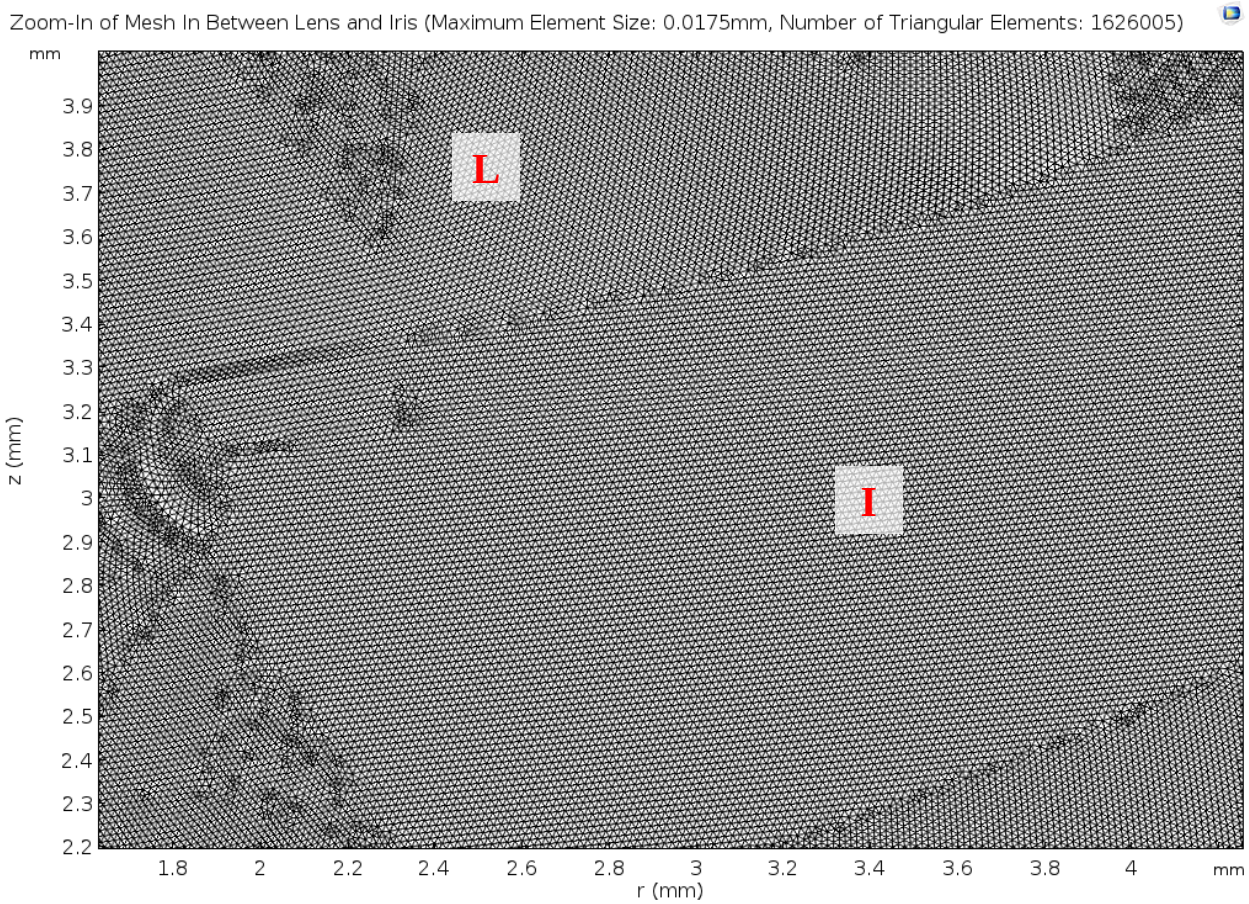

Figure A6. Zoom-In of Mesh in Between Lens and Iris. Lens (L); iris (I). The maximum mesh element size is 0.0175mm.

13.8.2 Degrees of Freedom

Pressure (comp1.p): 2691219
Concentration (comp1.c2): 814387 (plus 15440 internal DOFs)
Temperature (comp1.T): 3254778 (plus 30785 internal DOFs)
Velocity field (comp1.u): 113680 (plus 1 internal DOFs)
Pressure (comp1.p2): 56840
Total: 6930904 (plus 46226 internal DOFs)

13.8.3 CPU and Memory

Total Runtime (1 run) = 591s + 50s + 1704s = 2345s = 39 minutes, 5 seconds

Physical memory usage (Study 1 of 3) = 11.04 GB
Physical memory usage (Study 2 of 3) = 6.46 GB
Physical memory usage (Study 3 of 3) = 5.28 GB

Virtual memory usage (Study 1 of 3) = 12.9 GB
Virtual memory usage (Study 2 of 3) = 8.04 GB

Virtual memory usage (Study 3 of 3) = 6.47 GB
========== Opened Group03_final.mph ==========
<---- Compile Equations: Stationary in Study 1/Solution 1 (sol1) ----------
Started at 9-May-2018 19:29:29.
Geometry shape order: Linear
Running on Intel(R) Core(TM) i7-6700 CPU at 3.40 GHz.
Using 8 cores on 1 socket.
Available memory: 16.27 GB.
Time: 7 s.
Physical memory: 1.73 GB
Virtual memory: 1.89 GB
Ended at 9-May-2018 19:29:35.
----- Compile Equations: Stationary in Study 1/Solution 1 (sol1) ---------->
<---- Stationary Solver 1 in Study 1/Solution 1 (sol1) ----------
Started at 9-May-2018 19:29:39.
Segregated solver
Number of degrees of freedom solved for: 3425298 (plus 30786 internal DOFs).
Solution error estimates for segregated groups
0.00078, 2.7e-008
Residual error estimates for segregated groups
0.014, 1.6e-006
Solution time: 591 s. (9 minutes, 51 seconds)
Physical memory: 11.04 GB
Virtual memory: 12.9 GB
Ended at 9-May-2018 19:39:30.
----- Stationary Solver 1 in Study 1/Solution 1 (sol1) ---------->
==========
<---- Compile Equations: Stationary in Study 2/Solution 2 (sol2) ----------
Started at 9-May-2018 19:40:42.
Geometry shape order: Linear
Running on Intel(R) Core(TM) i7-6700 CPU at 3.40 GHz.
Using 8 cores on 1 socket.
Available memory: 16.27 GB.
Time: 5 s.
Physical memory: 2.81 GB
Virtual memory: 4.01 GB
Ended at 9-May-2018 19:40:47.
----- Compile Equations: Stationary in Study 2/Solution 2 (sol2) ---------->
<---- Stationary Solver 1 in Study 2/Solution 2 (sol2) ----------
Started at 9-May-2018 19:40:50.
Linear solver
Number of degrees of freedom solved for: 2691219.
Solution time: 50 s.
Physical memory: 6.46 GB
Virtual memory: 8.04 GB
Ended at 9-May-2018 19:41:40.

----- Stationary Solver 1 in Study 2/Solution 2 (sol2) ----------->

<---- Compile Equations: Time Dependent in Study 3/Solution 3 (sol3) -----------
Started at 9-May-2018 19:42:22.
Geometry shape order: Linear
Running on Intel(R) Core(TM) i7-6700 CPU at 3.40 GHz.
Using 8 cores on 1 socket.
Available memory: 16.27 GB.
Time: 5 s.
Physical memory: 3.25 GB
Virtual memory: 4.21 GB
Ended at 9-May-2018 19:42:26.
----- Compile Equations: Time Dependent in Study 3/Solution 3 (sol3) ---------->
<---- Time-Dependent Solver 1 in Study 3/Solution 3 (sol3) ----------
Started at 9-May-2018 19:42:29.
Time-dependent solver (BDF)
Number of degrees of freedom solved for: 814387 (plus 15440 internal DOFs).
Solution time: 1704 s. (28 minutes, 24 seconds)
Physical memory: 5.28 GB
Virtual memory: 6.47 GB
Ended at 9-May-2018 20:10:53.
----- Time-Dependent Solver 1 in Study 3/Solution 3 (sol3) ---------->

13.9 Mesh Convergence

Figure 9 is reproduced on the following page in full-page size for greater clarity.

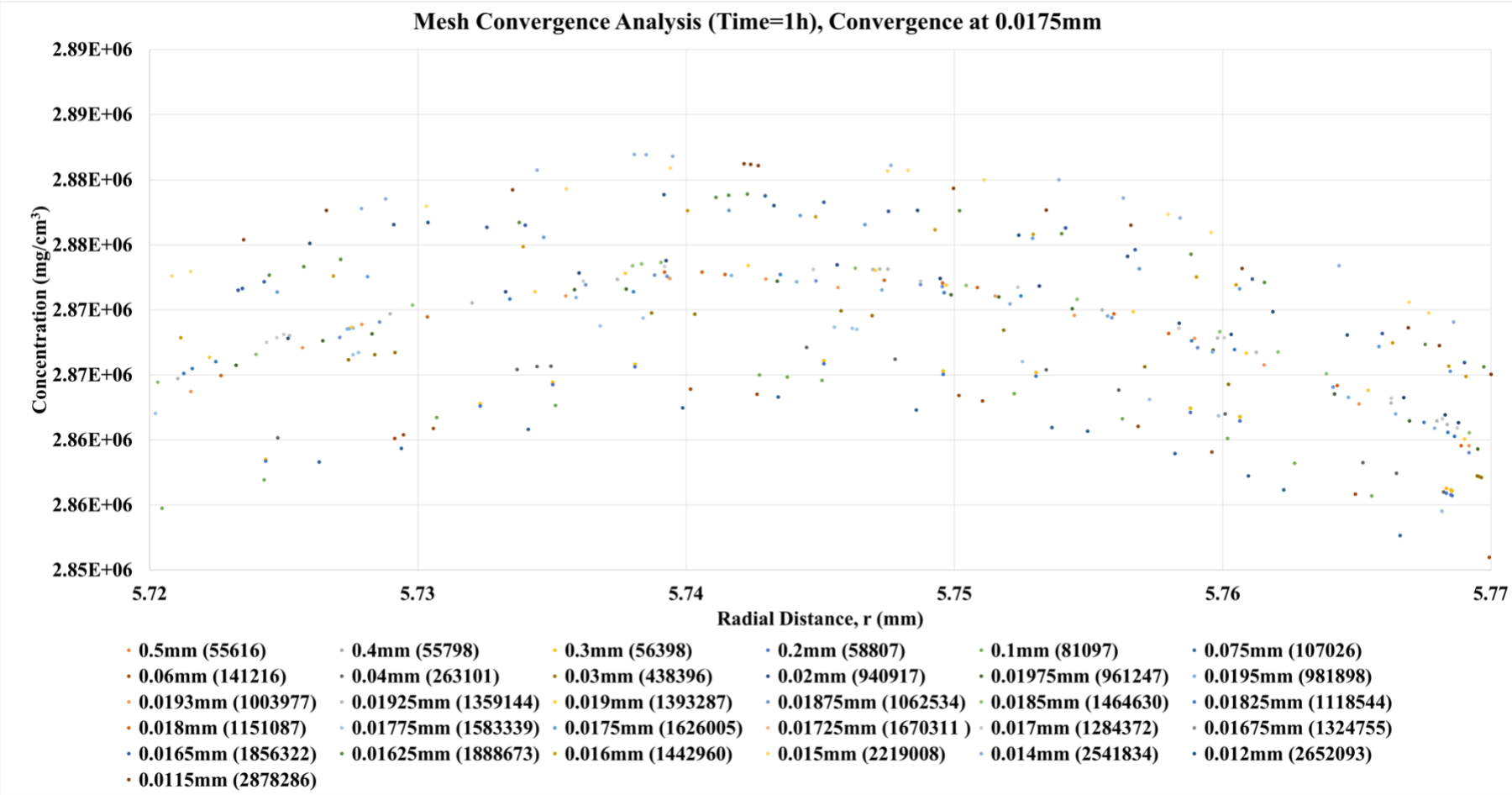

Figure 9. Mesh Convergence Analysis (Time=1h), Convergence at 0.0175mm. The number in parentheses indicates the total number of triangular mesh elements in the mesh corresponding to the specific maximum mesh element size. For each maximum mesh element size, we plotted Ofloxacin concentration along a 2D Cut-Line (from (0, 2.5) to (6.445, 2.5)). This plot can be divided into three broad bands: the smallest mesh sizes (0.0115mm-0.0175mm) form the topmost band, intermediate mesh sizes (0.01775mm-0.03mm) form the middle band, the largest mesh sizes (0.04mm-0.5mm) form the bottom band.

13.10 Optimization

The complete objective function is as follows:

$$J = \sum_{i=1}^{12244} F_C(c_i) + \sum_{j=1}^{8405} F_R\left(c_j\right) \tag{19}$$

where

$$F_C(c_i) = \begin{cases} 0, & if\ c_i < MIC_{90} \\ 1, & if\ MIC_{90} \le c_i \le 2200mg/m^3 \\ -\dfrac{c_i}{2200mg/m^3}, & if\ c_i > 2200mg/m^3 \end{cases}$$

$$F_R(c_j) = \begin{cases} -\dfrac{MIC_{90}}{c_r}, & if\ c_j < MIC_{90} \\ 1, & if\ c_j \ge MIC_{90} \end{cases}$$

$$MIC_{90} = \begin{cases} 250mg/m^3, & Escherichia\ coli \\ 1000mg/m^3, & Staphylococcus\ aureus \\ 2000mg/m^3, & Streptococcus\ pneumoniae \end{cases}$$

F_C is the sub-function that applies to all 12244 nodes in the cornea; c_i refers to Ofloxacin concentration at the i^{th} node in the cornea. F_R is the sub-function that applies to all 8405 nodes in the retina; c_j refers to Ofloxacin concentration at the j^{th} node in the retina.

The toxic threshold level of Ofloxacin in the cornea is $2200mg/m^3$ [14]. There is negligible retinal toxicity of Ofloxacin [20].

Table 7. Objective Function Values for $MIC_{90} = 250 mg/m^3$.

Case	Initial Mass (mg)	Diffusivity (m^2/s)	t=1h	t=8h
1	0.5	$3.11 \cdot 10^{-9}$	-7613.0291	-8405
2	0.5	$3.11 \cdot 10^{-10}$	-149625.24	-96768.292
3	0.5	$3.11 \cdot 10^{-11}$	-99299.33	-86565.268
4	0.5	$3.11 \cdot 10^{-12}$	-131845.09	-351291.28
5	1.2	$3.11 \cdot 10^{-9}$	-9554.58	3850
6	1.2	$3.11 \cdot 10^{-10}$	-36888.3	-19743.1
7	1.2	$3.11 \cdot 10^{-11}$	-236071	-218326
8	1.2	$3.11 \cdot 10^{-12}$	-315792	-854867
9	3	$3.11 \cdot 10^{-9}$	-12963.9	8294
10	3	$3.11 \cdot 10^{-10}$	-90457.6	-55203.4
11	3	$3.11 \cdot 10^{-11}$	-587489	-558421
12	3	$3.11 \cdot 10^{-12}$	-788077	-2149776
13	5	$3.11 \cdot 10^{-9}$	-17705.2	9628.773
14	5	$3.11 \cdot 10^{-10}$	-149625	-96768.3
15	5	$3.11 \cdot 10^{-11}$	-977976	-936306
16	5	$3.11 \cdot 10^{-12}$	-1315077	-3588563

Table 8. Objective Function Values for $MIC_{90} = 1000 mg/m^3$.

Case	Initial Mass (mg)	Diffusivity (m^2/s)	t=1h	t=8h
1	0.5	$3.11 \cdot 10^{-9}$	-7613.0291	-8405
2	0.5	$3.11 \cdot 10^{-10}$	-149625.24	-96768.292
3	0.5	$3.11 \cdot 10^{-11}$	-99299.33	-86565.268
4	0.5	$3.11 \cdot 10^{-12}$	-131845.09	-351291.28
5	1.2	$3.11 \cdot 10^{-9}$	-9554.58	3850
6	1.2	$3.11 \cdot 10^{-10}$	-36888.3	-19743.1
7	1.2	$3.11 \cdot 10^{-11}$	-236071	-218326
8	1.2	$3.11 \cdot 10^{-12}$	-315792	-854867
9	3	$3.11 \cdot 10^{-9}$	-12963.9	8294
10	3	$3.11 \cdot 10^{-10}$	-90457.6	-55203.4
11	3	$3.11 \cdot 10^{-11}$	-587489	-558421
12	3	$3.11 \cdot 10^{-12}$	-788077	-2149776
13	5	$3.11 \cdot 10^{-9}$	-17705.2	9628.773
14	5	$3.11 \cdot 10^{-10}$	-149625	-96768.3

15	5	$3.11 \cdot 10^{-11}$	-977976	-936306
16	5	$3.11 \cdot 10^{-12}$	-1315077	-3588563

Table 9. Objective Function Values for $MIC_{90} = 2000 mg/m^3$.

Case	Initial Mass (mg)	Diffusivity (m^2/s)	t=1h	t=8h
1	0.5	$3.11 \cdot 10^{-9}$	-7613.0291	-8405
2	0.5	$3.11 \cdot 10^{-10}$	-149625.24	-96768.292
3	0.5	$3.11 \cdot 10^{-11}$	-99299.33	-86565.268
4	0.5	$3.11 \cdot 10^{-12}$	-131845.09	-351291.28
5	1.2	$3.11 \cdot 10^{-9}$	-9554.58	3850
6	1.2	$3.11 \cdot 10^{-10}$	-36888.3	-19743.1
7	1.2	$3.11 \cdot 10^{-11}$	-236071	-218326
8	1.2	$3.11 \cdot 10^{-12}$	-315792	-854867
9	3	$3.11 \cdot 10^{-9}$	-12963.9	8294
10	3	$3.11 \cdot 10^{-10}$	-90457.6	-55203.4
11	3	$3.11 \cdot 10^{-11}$	-587489	-558421
12	3	$3.11 \cdot 10^{-12}$	-788077	-2149776
13	5	$3.11 \cdot 10^{-9}$	-17705.2	9628.773
14	5	$3.11 \cdot 10^{-10}$	-149625	-96768.3
15	5	$3.11 \cdot 10^{-11}$	-977976	-936306
16	5	$3.11 \cdot 10^{-12}$	-1315077	-3588563

14 References

[1] L. P. Jervis, "A Summary of Recent Advances in Ocular Inserts and Implants," *J. Bioequivalence Bioavailab.*, vol. 9, no. 1, pp. 320–323, Feb. 2017.

[2] M. E. Kavousanakis, N. G. Kalogeropoulos, and D. T. Hatziavramidis, "Computational modeling of drug delivery to the posterior eye," *Chem. Eng. Sci.*, vol. 108, pp. 203–212, Apr. 2014.

[3] P. W. Morrison and V. V. Khutoryanskiy, "Advances in ophthalmic drug delivery," *Ther. Deliv.*, vol. 5, no. 12, pp. 1297–1315, Dec. 2014.

[4] F. A. Maulvi, T. G. Soni, and D. O. Shah, "A review on therapeutic contact lenses for ocular drug delivery," *Drug Deliv.*, vol. 23, no. 8, pp. 3017–3026, Oct. 2016.

[5] P. Bansal, S. Garg, Y. Sharma, and P. Venkatesh, "Posterior Segment Drug Delivery Devices: Current and Novel Therapies in Development," *J. Ocul. Pharmacol. Ther.*, vol. 32, no. 3, pp. 135–144, Jan. 2016.

[6] Y. Shikamura, Y. Yamazaki, T. Matsunaga, T. Sato, A. Ohtori, and K. Tojo, "Hydrogel Ring for Topical Drug Delivery to the Ocular Posterior Segment," *Curr. Eye Res.*, vol. 41, no. 5, pp. 653–661, May 2016.

[7] Y. Shikamura, A. Ohtori, and K. Tojo, "Drug penetration of the posterior eye tissues after topical instillation: in vivo and in silico simulation," *Chem. Pharm. Bull. (Tokyo)*, vol. 59, no. 10, pp. 1263–1267, 2011.

[8] F. Zhang, H. Chen, and Y. Huang, "Computer modeling of drug delivery in the anterior human eye after subconjunctival and episcleral implantation," *Comput. Biol. Med.*, vol. 89, pp. 162–169, Oct. 2017.

[9] C.-W. Lin and F. Yuan, "Numerical simulations of ethacrynic acid transport from precorneal region to trabecular meshwork," *Ann. Biomed. Eng.*, vol. 38, no. 3, pp. 935–944, Mar. 2010.

[10] J. J. Heys and V. H. Barocas, "A Boussinesq Model of Natural Convection in the Human Eye and the Formation of Krukenberg's Spindle," *Ann. Biomed. Eng.*, vol. 30, no. 3, pp. 392–401, Mar. 2002.

[11] W. D. Mahathanthila, "Modeling of Drug Delivery to the Human Eye," California State Polytechnic University, Pomona, 2017.

[12] R. K. Balachandran and V. H. Barocas, "Computer Modeling of Drug Delivery to the Posterior Eye: Effect of Active Transport and Loss to Choroidal Blood Flow," *Pharm. Res.*, vol. 25, no. 11, pp. 2685–2696, Nov. 2008.

[13] S. J. Ahn *et al.*, "Use of Rabbit Eyes in Pharmacokinetic Studies of Intraocular Drugs," *JoVE J. Vis. Exp.*, no. 113, pp. e53878–e53878, Jul. 2016.

[14] A. Smith, P. M. Pennefather, S. B. Kaye, and C. A. Hart, "Fluoroquinolones: place in ocular therapy," *Drugs*, vol. 61, no. 6, pp. 747–761, 2001.

[15] A. Bonfiglio, A. Lagazzo, R. Repetto, and A. Stocchino, "An experimental model of vitreous motion induced by eye rotations," *Eye Vis.*, vol. 2, p. 10, Jun. 2015.

[16] X. Zhang *et al.*, "Bulbar Conjunctival Thickness Measurements With Optical Coherence Tomography in Healthy Chinese Subjects," *Invest. Ophthalmol. Vis. Sci.*, vol. 54, no. 7, pp. 4705–4709, Jul. 2013.

[17] N. Tang *et al.*, "Thermal Conductivity of PAAm Hydrogel and its Crosslinking Effect," *ArXiv170501417 Cond-Mat*, May 2017.

[18] K. Ishikiriyama and M. Todoki, “Heat capacity of water in poly(methyl methacrylate) hydrogel membrane for an artificial kidney,” *J. Polym. Sci. Part B Polym. Phys.*, vol. 33, no. 5, pp. 791–800, Apr. 1995.
[19] A. F. R. Pimenta, J. Ascenso, J. C. S. Fernandes, R. Colaço, A. P. Serro, and B. Saramago, “Controlled drug release from hydrogels for contact lenses: Drug partitioning and diffusion,” *Int. J. Pharm.*, vol. 515, no. 1–2, pp. 467–475, Dec. 2016.
[20] R. G. Cohen, M. Raizman, C. Callina, and M. Lahav, “Retinal Safety of Oral and Topical Ofloxacin in Rabbits,” *J. Ocul. Pharmacol. Ther.*, vol. 13, no. 4, pp. 369–379, Aug. 1997.